LAWRENCE
LIVERMORE
NATIONAL
LABORATORY

UCRL-TR-206721

Neutron and Charged-Particle Induced Cross Sections for Radiochemistry in the Region of Iodine and Xenon

R. D. Hoffman, F. S. Dietrich, R. Bauer, K. Kelley, M. Mustafa

September 22, 2004

This work was performed under the auspices of the U.S. Department of Energy by University of California, Lawrence Livermore National Laboratory under Contract W-7405-Eng-48.

UCRL-TR-206721

Neutron and Charged-Particle Induced Cross Sections for Radiochemistry in the Region of Iodine and Xenon

R. D. Hoffman, F. S. Dietrich and R. Bauer
Nuclear Theory and Modeling Group
Physics and Advanced Technologies, N-Division
Lawrence Livermore National Laboratory
Livermore, CA 94550
rdhoffman@llnl.gov

K. Kelley[1] and M. Mustafa
Nuclear and Defense Technologies, AX-Division
Lawrence Livermore National Laboratory
Livermore, CA 94550

ABSTRACT

We have developed a set of modeled nuclear reaction cross sections for use in radiochemical diagnostics. Systematics for the input parameters required by the Hauser-Feshbach statistical model were developed and used to calculate neutron and proton induced nuclear reaction cross sections in the mass region of iodine and xenon ($52 \leq Z \leq 54$, $71 \leq N \leq 76$).

Subject headings: Nuclear cross sections, Radiochemistry, Nuclear Physics

1. Introduction

1.1. Radiochemistry

Various aspects of nuclear explosive device performance can be determined through the use of radiochemistry. During the UGT (Under Ground Test) Program, select naturally occurring elements were loaded into a device prior to a test and their activation products subsequently retrieved for counting, typically with gamma-ray detectors. The products are measured as isotopic ratios (such as $^{87}Y/^{88}Y$ produced from a stable isotope of the naturally occurring element). From the measured activity and prior knowledge of the amount of loaded detector material, performance aspects could be inferred by comparing the measured isotope ratios with those calculated using neutron and charged-particle fluences from one of the design codes and group-averaged cross section sets that have been prepared for this purpose.

This is the second in a series of papers that will detail a collaborative effort between AX-Division and N-Division (PAT) to update and improve the existing charged particle cross section detector sets. This paper will be devoted to the iodine-xenon detector set. The first paper detailed the modeling of the bromine-krypton detector set (Hoffman *et al.* 2004). We restrict our discussion to unclassified data related to the modeling effort. A separate classified document will discuss Stockpile Stewardship applications.

[1]Department of Physics, University of California, Davis Davis, CA 95616

Contents

List of Figures

List of Tables

1.2. Iodine Detector Set

1.2.1. Current Detector Set

Over the last 40 years a number of detector sets have been developed at LLNL and LANL. Twenty-three neutron threshold detector sets and five charged particle sets are currently available. The Iodine set (II0391) is a charged particle set used to calculate activation of ^{127}Xe ($\tau_{1/2}$ = 36.4 d) from stable ^{127}I, and consists of six reactions, two charged particle reactions based on experiment (West *et al.* 1993) and four neutron induced reactions. Of these, one is based on experimental data, two are from calculations, and one was estimated. The set is summarized in Table 1 and can be accessed on the world wide web, see http://nuclear.llnl.gov/CNP/nads/main.html.

Set→	I0391
Experimental	^{127}I(p,n)^{127}Xe ^{127}I(d,2n)^{127}Xe ^{127}I(n,γ)^{128}I
Estimated	^{127}I(n,2n)^{126}I ^{127}Xe(n,2n)^{126}Xe
Copied	^{127}Xe(n,γ)^{128}Xe

Table 1: Cross sections: II0391 set

1.2.2. The Need for a New Detector Set

The motivations for revisiting the detector sets for radiochemistry are many. The current sets were often developed based on "best guess" and "experience" from a limited amount of experimental data over a 40 year period. Often a single measurement at 14 MeV guided the evaluation of a critical (n,2n) cross section, with an assumed shape that would rise from a calculated threshold, and then adjusted to match the experimental point at 14 MeV. This was actually done for both (n,2n) cross sections included in the II0391 set.

For the set of interest here (II0391), a total of three reaction cross sections were estimated and/or extrapolated from data spanning energies up to 1 MeV. Of these, suggestions to scale them (to correct for photon intensities in use from Test Program measurements), have yet to be made to the charged particle production cross sections. Many are still based on preliminary data. Additionally, in 1991, only three cross sections could be compared to experimental data (Nethaway 1998).

Of the remaining reactions, many were modeled or estimated, but often only over a limited energy range. Beyond this range they were extrapolated. For example, the (n,2n) reactions on ^{127}I and ^{127}Xe were estimated from an assumed maximum cross section (1.74 barns at 14 MeV) and a standard shape rising from threshold. The (n,γ) cross section on ^{127}I was based on experimental data from three sources with educated guesses for extrapolations to both lower and higher energies. The critical ^{127}Xe(n,γ)^{128}Xe cross section was actually copied from the estimated ^{127}I(n,γ)^{128}I cross section.

In the decade since this cross section set was last evaluated, many new cross section measurements have been performed, and several efforts have been made to develop consistent approaches to modeling nuclear reaction cross section (RIPL 1998). The basic nuclear structure data has been greatly improved. Finally, there are more accurate methods of calculating and estimating cross sections for which we have no data.

1.2.3. Proposed New Iodine Detector Set

We consider as targets all isotopes of the elements Te, I, and Xe ($52 \leq Z \leq 54$) with neutron numbers $71 \leq N \leq 76$ (including any long-lived isomers with half-lives greater than 1 μs), and have calculated nuclear reaction cross sections for incident neutrons and protons on these targets with laboratory incident particle energies ranging from 0.01 keV to 20 MeV. These compound systems are then allowed to decay through the reaction channels shown in Table 2 (see Appendix A.1).

The reason for including many more isotopes than were included in the original sets is to account for the various possible *destruction* reactions that are significant in this mass range. In general, the current RADCHEM detector sets, and especially the charged-particle sets, were developed with special attention paid to the *production* reactions. We have also included the isomers as targets, which were not included in the original sets, in order to gauge the sensitivity of the set to their inclusion. The activation product ^{127}Xe, as measured in the UGT Program, only considers decay to the ground state. We actually delivered to A-Program two detector sets, the *Activation*

set, which includes only reactions that couple the ground states of all the isotopes considered, and the *Full set*, which included the isomers as well.

Another important reason for considering a larger range of nuclei is to compare our calculated cross sections to the many measured cross sections available for the stable isotopes of antimony, tellurium, and cesium. Our goal is to develop a consistent set that reproduces, as closely as possible, measured cross sections on targets in the *local region of interest*. To do this we develop *local systematics* for the many input quantities used in the theoretical reaction modeling calculations. These systematics are based on experimental data that are often only available for compound nuclear systems formed from a stable target plus a neutron. Of course, we use experimental data whenever it is available, but reactions proceeding through unstable systems are unavoidable in radiochemistry. Short of developing new experimental techniques to measure cross sections on unstable targets, our only hope of reproducing measured activity from UGT shots, and addressing the uncertainty associated with the nuclear cross sections, is to develop cross section sets that reproduce well the measured cross sections in the region of interest.

In §2 we describe the theoretical techniques used in the modeling effort. §3 describes the input parameters. §4 gives results. We conclude with §5.

2. Nuclear Reaction Theory

2.1. Reaction Mechanisms

Conceptually, we consider nuclear reaction mechanisms to be of two general types, direct processes and compound processes. Direct processes can be pictured as simple interactions of the incident particle with the nuclear potential of the target nucleus. They proceed on a rapid time scale (of order $\sim 10^{-22}$ s), and the reaction products are often highly peaked in the incident particle direction. Compound processes are pictured as complicated interactions proceeding over a much longer timescale ($10^{-15} - 10^{-18}$ s) in which the reaction is mediated by the formation of a "compound nucleus", with the excitation energy of the incident particle being statistically "shared" with the ensemble of nucleons in the target over all energetically allowed degrees of freedom. The reaction products are largely isotropic. Compound nuclear reactions proceed through resonances, which correspond to nuclear states above the bound region, while direct reactions proceed through smooth potential terms. Other intermediate reaction mechanisms may exist between these two extremes. We refer to these as "pre-compound" nuclear processes. Over the energy range of interest to this project, a few keV to 20 MeV, we will consider pre-compound and compound nuclear processes, with the pre-compound reactions operating principally above 10 MeV of incident particle excitation energy.

2.2. Hauser-Feshbach Statistical Model

A traditional theoretical approach to compound nuclear reactions is the statistical or Hauser-Feshbach model. This model is valid only for high level densities in the compound nucleus, allowing one to use energy averaged transmission coefficients T, which describe absorption via an imaginary part in the (optical) nucleon-nucleus potential (for details see Mahaux and Weidenmüller 1979). For the reaction I (in state μ) $+j \rightarrow k +$ L (in state ν), with $\mathrm{I}^{\nu} + j$ interacting with center-of-mass energy E_j^{μ} (in MeV), the average cross section is given by

$$\sigma_{jk}^{\mu\nu}(E_j^{\mu}) = \frac{\pi \lambda\!\!\!^{-2}_j}{g_I^{\mu} g_j} \sum_{J,\pi} g_J \frac{T_j^{\mu}(J^{\pi}) T_k^{\nu}(J^{\pi})}{T_{tot}(J^{\pi})} W(J^{\pi}) \tag{1}$$

where the summation extends over all compound nuclear spins and parities J^{π}, μ and ν are states in the target and product (=0 for the ground state, 1 for the 1^{st} excited state, etc.). The cross section has units of area, described by $\pi \lambda\!\!\!^{-2}_j = 0.6566(\hat{A}_j E_j^{\mu})^{-1}$ barns, with $\hat{A}_j = (A_I A_j)/(A_I + A_j)$ being the reduced mass in atomic mass units and E_j^{μ} is the center of mass energy in units of MeV. $\lambda\!\!\!^{-}_j$ is the wavelength related to the wave number k_j in the target plus incident particle channel by $\lambda\!\!\!^{-}_j = 1/k_j$ The statistical weights are given by $g_y^x = (2J_y^x + 1)$. Items without superscripts refer to the compound nucleus.

The transmission coefficients in the numerator are given by $T_j^{\mu}(J^{\pi}) =$ the total transmission coefficient for forming the state J^{π} in the compound nucleus $I^{\mu} + j$ at energy E_j^{μ}. Likewise, $T_k^{\nu}(J^{\pi})$ is the same as $T_j^{\mu}(J^{\pi})$ but for the pair $L^{\nu} + k$ at

energy E_k^ν. Implicit in these definitions is a sum over all possible $l-$waves and channel spins, i.e.

$$T_j^\mu(J^\pi) = \sum_{l,s} T_j^\mu(J^\pi, l, s) \qquad (2)$$

where l is any partial wave number (orbital angular momentum) that can couple the state μ to the compound nuclear state having spin and parity J^π subject to quantum mechanical selection rules and s is the vector sum of the spins J_I^μ and J_j. Hence s takes on all integer (or half-integer) numbers from $|J_I^\mu - J_j|$ to $J_I^\mu + J_j$.

T_{tot} represents the sum of transmission coefficients over all possible decay channels (i.e. for all particles and photons). The cross section for the formation of species L, regardless of its state ν, is obtained by summing Eq. [1] over all bound states ν of L for which the reaction is energetically allowed.

When evaluating these sums, if energies become of interest which exceed the highest discrete excited state for which energy, spin, and parity are explicitly known, a nuclear level density formula must be employed. Specifically, the definitions for the transmission coefficients $T_j(J^\pi)$, $T_k(J^\pi)$, and $T_{tot}(J^\pi)$ must be modified, for example:

$$T_k(J^\pi) = \sum_{\nu=0}^{\omega} T_k^\nu(J^\pi) + \int_{\xi_L^\omega}^{\xi_L^{max}} \int_{J^\nu \pi^\nu} T_k^\nu(\xi_L^\nu, J^\pi)\rho(\xi_L^\nu, J^\nu, \pi^\nu) d\xi_L^\nu d\pi^\nu dJ^\nu$$

where for the nucleus L, ξ_L^ω is the energy of the highest excited state, ω, of known energy, spin, and parity; $\xi_L^{max} = E_k^0 = E_j^0 + Q_{jk}$ is the maximum excitation energy available, and $\rho(\xi_L^\nu, J^\nu, \pi^\nu)$ is the density of states per unit energy of spin and parity J^ν and π^ν at the excitation energy ξ_L^ν. The above integral approximates a summation and is subject to the same quantum mechanical restrictions implied in the definition of the transmission function.

2.3. Width Fluctuations

In addition to the ingredients required for Eq. [1], like the transmission coefficients for particles and photons or the level densities, width fluctuation corrections (WFC) have to be employed as well. They define the correlation factors with which all partial channels of incoming particle j and outgoing particle k, passing through excited state (E, J, π), have to be multiplied. The major effect is to enhance the elastic channel and accordingly decrease the other open channels. They are most often observed at or near channel opening energies when i.e. a (p,γ) and a (p,n) channel compete and the weaker (p,γ) channel is enhanced. Above a few MeV of excitation energy, when many competing channels are open, WFC's can be neglected.

The exact expression for the WFC, obtained with the Gaussian orthogonal ensemble (GOE) approach, requires the evaluation of a triple integral and to date has been considered much to costly to apply in nuclear cross section calculations. Several approximations have been developed, the most popular ones are the Moldauer model (Moldauer 1976), and the HRTW model (Hofmann *et al.* 1975). We use the Moldauer model approximation in this study. For a detailed description of the full (GOE) treatment and a comparison with the Moldauer and HRTW approximation models mentioned above, see (Hilaire Lagrange & Koning 2003).

2.4. Pre-Compound Processes

For incident particle energies starting around 10 MeV, pre-compound processes become important. The pre-compound cross section is subtracted from the total cross section of the first compound nucleus, and is usually unimportant for subsequent compound nuclei. Here we describe equilibration of the compound nuclear system in terms of a simple exciton model. In the pre-equilibrium stage of the reaction particle emission is assumed to be the only decay mode. For the equilibration portion of the first chance particle or photon emission as well as for first chance fission, the width fluctuated Hauser Feshbach formula (Eq. [1]) is applied. All subsequent (higher chance) processes are treated as sequential evaporation steps.

2.5. The STAPRE Hauser-Feshbach Reaction Code

We adopt the statistical model code STAPRE (STAatistical-PREequilibrium) to model our cross sections (Uhl & Strohmaier 1976). It embod-

ies all of the physical models discussed above. The version of the code we use is STAPRE-H95 (Avrigeanu & Avrigeanu 1976), available from the NEA web site. We have made several modifications, primarily to the level density routines. Prior versions of the code were used to develop parts of the existing RADCHEM data sets (Vonach 1982).

In the following we discuss the important ingredients of statistical model calculations, and the methods utilized to estimate them. These are the requisite nuclear structure data (energies, spins, and parities of the ground states and all known excited states, as well as detailed branching ratios for the gamma-ray cascade from excited to low-lying states), the width fluctuation corrections, the pre-compound cross section, the particle and γ-transmission coefficients, and the nuclear level densities of all nuclei involved in the reaction. The reliability of such calculations is chiefly determined by the accuracy with which these components can be evaluated.

3. Inputs Required for the Hauser-Feshbach Model

3.1. Nuclear Structure Data

3.1.1. Nuclear Masses and J^π Assignments

We adopt for nuclear masses the experimental mass excess values of (Möller *et al.* 1995). Spin and parity assignments are from the Evaluated Nuclear Structure Data File (ENSDF 2003). We present in Table 3 (Appendix A.2) the binding energies (in MeV) calculated from the adopted masses, the ground state spins and parities, and the separation energies for neutrons, protons, alpha-particles, and deuterons for the nuclei included in this study. In Table 4 (Appendix A.3), we provide Q-values for various cross sections that were calculated in this study.

3.1.2. Nuclear Level Schemes

The nuclear structure data needed to model the gamma-ray cascade in this study was adopted from the file BUDAPEST.DAT (RIPL 1998). For the antimony, tellurium, iodine and xenon isotopes, additional evaluation was performed (Bauer 2002). Shown in Appendix A.4 are a selection of the modified adopted nuclear levels, including level energy, spin and parity assignments, and their gamma-cascade branching ratios. The number of levels adopted for each nucleus is given as the quantity "N" in Table 5 (Appendix A.5). For the unmodified isotopes, this was the number for which energy spin and parity were unambiguously assigned in the BUDAPEST file.

3.2. Transmission Coefficients

3.2.1. Transmission Coefficients for Particles

We restrict our attention in this modeling effort to reactions with incident neutrons and protons. For the charged particle cross sections to be included in the new iodine set, we adopt experimental results for the ^{127}I(p,n)^{127}Xe reaction (West *et al.* 1993). We present modeled results for (p,n) and (p,2n) reactions on all included isotopes for elements Te, I, and Xe. Ideally, one would prefer (d,n) and (d,2n) cross sections on all targets in the set. However, for use as a radiochemical detector set, the omission is not important, as only ^{127}I is loaded, and any abundance produced during activation will be so small that the impact on the deuterium abundance (compared to other fusion reactions) will be negligible.

3.2.2. The Optical Potential of Koning and Delaroche

For the calculation of the particle transmission coefficients, we used the optical model developed by (Koning & Delaroche 2001). Although they have tuned their parameters to fit data for many different species (see their Tables 6 and 7), we decided to use the Global nucleon-nucleon optical model potential (OMP), as it gives a very satisfactory fit to measured total cross section data for neutrons and protons in the range of interest to us (e.g. Sb-Cs). In specific, we adopted the potential depth parameters and Fermi energies for the neutron and proton global OMP defined in their Section 5.2, tables 14 and 15. The particle transmission coefficients were generated by the optical model code ECIS-95 (Raynal 1996). Although designed for coupled channel calculations, we used the code in a spherical optical model mode.

3.2.3. Evaluation of the Optical Potential

We present in Figure (1) results of the Koning & Delaroche optical model compared to measured total neutron cross sections. The comparisons in

Figure 1 are for total neutron cross sections on ^{127}I and ^{133}Cs. Other experimental total neutron cross section data in this region generally consists of a single point at roughly 14 MeV. In each instance, the optical model closely replicated the experimental data. No total proton cross section data was available in this region. For additional comparisons, see (Koning & Delaroche 2001).

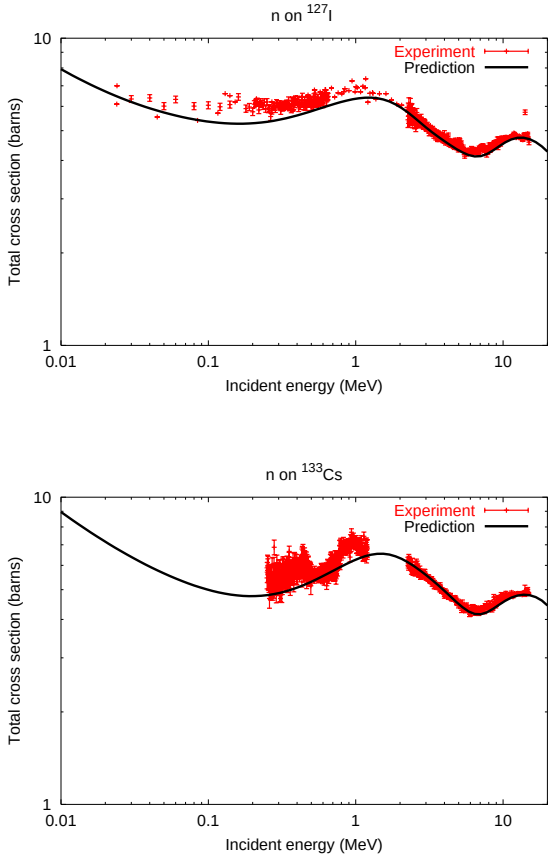

Fig. 1.— Total measured neutron cross sections vs Koning-Delaroche for ^{127}I+n and ^{133}Cs+n.

3.2.4. Transmission Coefficients for Photons

For the calculation of the gamma ray transmission coefficients, we use a simple model where the transmission coefficient depends only on the multipole type (XL) and the transition energy (ϵ), as encoded in STAPRE (Avrigeanu & Avrigeanu 1976). They are related to the gamma ray strength function $f^{\gamma}_{XL}(\epsilon)$ by

$$T^{\gamma}_{XL}(\epsilon) = 2\pi\epsilon^{2L+1} f^{\gamma}_{XL}(\epsilon) \tag{3}$$

The energy dependence of the strength function was determined using the GDR model with Lorentz line shapes. In particular, the E1 strength function is given by

$$f^{\gamma}_{E1}(\epsilon) = \mathcal{N}\zeta\sigma_G \frac{\Gamma_G^2\epsilon}{\left(\epsilon^2 - E_G^2\right)^2 + \left(\Gamma_G\epsilon\right)^2} \ (\mathrm{MeV}^{-3}) \tag{4}$$

where E_G, Γ_G, and σ_G are the energy, width, and peak cross section of the Giant Dipole Resonance given in MeV and mb. The constant ζ is 8.674×10^{-8} mb^{-1}·MeV^{-2}. The GDR parameters are given by

$$\begin{aligned} E_G &= \frac{80 \text{ MeV}}{A_C^{1/3}} \\ \Gamma_G &= 5 \text{ MeV} \\ \sigma_G &= A_C \frac{13 \text{ mb}}{5} \end{aligned} \tag{5}$$

where A_C is the mass number of the compound nucleus. We use only one E1 resonance. We also include M1, E2, and M2 transitions. Their transmission coefficients are simply proportional to ϵ^{2L+1}, and therefore their strength functions are constants. In particular,

$$\begin{aligned} f^{\gamma}_{M1}(\epsilon) &= \frac{0.31}{A_C^{2/3}} f^{\gamma}_{E1}(S_n) \\ f^{\gamma}_{E2}(\epsilon) &= 7.2\times10^{-7} A_C^{2/3} f^{\gamma}_{E1}(S_n) \\ f^{\gamma}_{M2}(\epsilon) &= 2.2\times10^{-7} f^{\gamma}_{E1}(S_n) \end{aligned} \tag{6}$$

where S_n is the neutron separation energy. In all cases, E1 is the dominant radiation.

The factor $\mathcal{N}$ appearing in equation 4 is a normalization constant, determined by fitting the average total s-wave radiation width at the neutron binding energy,

$$\begin{aligned} \langle\Gamma_\gamma\rangle_0 &= \frac{J+1}{2J+1}\langle\Gamma_\gamma\left(B_n, J+\frac{1}{2}\right)\rangle \\ &+ \frac{J}{2J+1}\langle\Gamma_\gamma\left(B_n, J-\frac{1}{2}\right)\rangle \end{aligned} \tag{7}$$

$$\Gamma_\gamma\left(E,J\right) = \frac{T_\gamma(E,J)}{2\pi\rho(E,J)} \ (\mathrm{meV})$$

(Uhl & Strohmaier 1976). Here, J is the spin of the target nucleus. The gamma-ray transmission coefficient is evaluated as in equation 3. Since the total s-wave radiation width is generally measured only for stable isotopes plus a neutron, we developed a systematic approach for estimating this value for the many unstable nuclei in our region of interest. The systematic values are determined by a least squares linear fit to experimental data, with separate systematics developed for even-Z even-N, even-Z odd-N, odd-Z even-N, and odd-Z odd-n nuclei (Figure 2). Unfortunately, no odd-Z even-N data was available in this region of interest, so we used the odd-Z odd-N systematic for all odd-Z nuclei. We do present data for higher neutron numbers and a systematic based on them, which indicates a higher average photon width when extrapolated to the region of N$\sim$ 73. There the percentage difference between the two systematics is $\sim 25\%$, which could allow for up to a 25% increase in a capture cross section (^{127}Xe(n,γ)^{128}Xe for example). Of course we used the experimental values for all systems that had measured average s-wave radiation widths.

3.3. Nuclear Level Densities

3.3.1. Level Density Models

Another important input to the statistical model code, especially for the capture reactions, is the nuclear level density. For this project, we have adopted a standardized, semi-empirical approach (Gilbert & Cameron 1965) which is numerically efficient, can be tied to experimental data, and is fairly accurate. The level density is described by two functions. Both are energy dependent, the second factor contains the spin dependence:

$$\rho\left(U,J\right)=\rho\left(U\right)f\left(U,J\right) \tag{8}$$

where $\rho(U)$ is the state density, with $U = E - \Delta$ the back-shifted energy. Δ is the so called "pairing energy", and J is the spin of the compound nucleus. We will further treat each of these in two ways, depending on the excitation energy of interest. The demarcation point will be roughly between the energy range of the known excited levels of a given compound nucleus (the low energy domain), and near (and above) the neutron binding energy (the high energy domain).

For the high energy domain, we describe the level density assuming a Fermi gas formula,

$$\rho\left(U\right)=\frac{\sqrt{\pi}}{12}\ \frac{\exp\left(2\sqrt{aU}\right)}{a^{1/4}U^{5/4}}\ \frac{1}{\sqrt{2\pi}\sigma} \tag{9}$$

$$f\left(U,J\right)=\frac{2J+1}{2\sigma^{2}}\ \exp\left[\frac{-\left(J+\frac{1}{2}\right)^{2}}{2\sigma^{2}}\right] \tag{10}$$

where $a(U, Z, N)$ is the level density parameter (in MeV^{-1}). The spin cutoff parameter σ^2 is defined as

$$\sigma^{2}=\lambda\sqrt{aU}A^{2/3} \tag{11}$$

The level density assumes an equal distribution of parity states. Note that at low excitation energy (for a positive back-shift), Eq. [9] diverges. At low energies, the nuclear level density is better described by a constant temperature formula:

$$\rho(E)\propto\exp\frac{E-E_{0}}{T} \tag{12}$$

The level density parameters can be calculated using experimental data. For the Fermi-gas state density (Eq. [9]), the level density parameter, $a(E)$, can be related to the average level spacing (D_0) near the neutron binding energy. The pairing energies used in the calculation of the back shifted energy are calculated as differences of binding energies (Bohr & Mottelson). The constant temperature parameters E_0 and T, can be chosen to provide a state density that goes through the low lying spectroscopic levels subject to the choice of a matching energy, E_x, chosen someplace between the high and low energy regions of interest, at which the two state densities match (point and slope). We describe below how we determined these parameters for all of the nuclei considered in this study.

3.3.2. Level Densities Above the Neutron Binding Energy

Our goal is to fit the level density parameter a in Eq. [9] to experimental data where available. We adopt an energy dependent form, $a(U, Z, N)$, (Iljinov *et al.* 1992), and begin by fixing the spin cutoff parameter and the pairing energies.

The Spin Cutoff Parameter

The spin cutoff parameter σ^2, Eq. 11, characterizes the spin distribution of the Fermi gas level

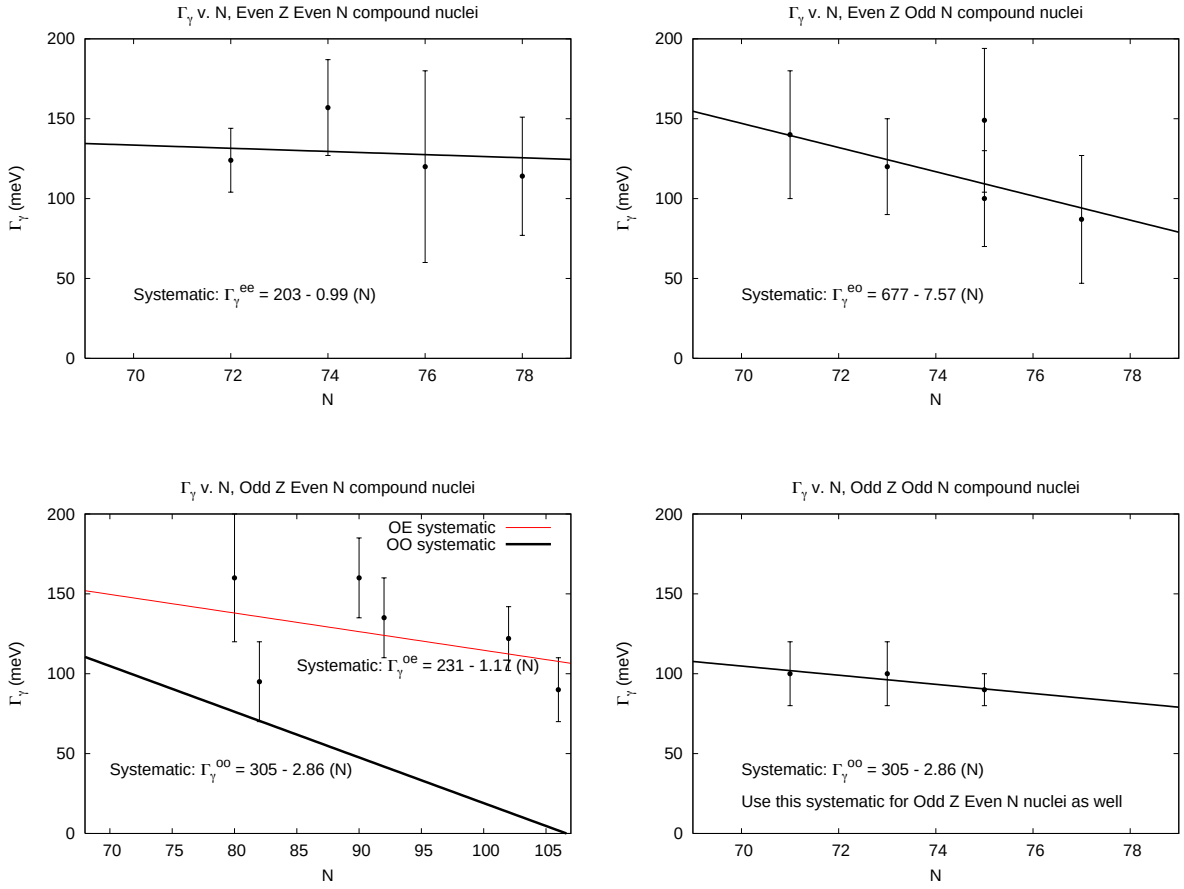

Fig. 2.— Systematics for average total s-wave radiation width.

density. It depends on the parameters a, the level density parameter, and λ, which determines the effective moment of inertia for the nucleus in question. In principle it could be determined by experiment, for example, by comparing ratios of cross sections leading to different isomers of the product nucleus (Keisch 1963). Because data like this is often sparse, especially in the limited regions of the periodic chart we are interested in, and because we are often interested in reactions that proceed on or through radioactive species where no such data exists, we must resort to models. In our analysis, we chose to fix $\lambda = 0.146$ in Eq. [11], as proposed by (Rauscher *et al.* 1997).

Pairing Energies

In determining the back-shift Δ, also known as the pairing energy, we used a slightly modified version of the method of Rauscher (Rauscher *et al.* 1997). The total pairing energy is equal to the sum of the proton and neutron pairing energies

$$\begin{aligned} \Delta(Z,N) &= \Delta_p + \Delta_n \\ \Delta_p(Z,N) &= E^G(Z,N) \\ &- \frac{1}{2}E^G(Z-1,N) \\ &- \frac{1}{2}E^G(Z+1,N) \\ \Delta_n(Z,N) &= E^G(Z,N) \\ &- \frac{1}{2}E^G(Z,N-1) \end{aligned} \tag{13}$$

$$- \quad \frac{1}{2}E^G\left(Z, N+1\right)$$

where $E^G\left(Z,N\right)$ is the binding energy of the nucleus (Z,N). For odd-Z nuclei, we take $\Delta_p = 0$, and for odd-N nuclei $\Delta_n = 0$. In calculating the binding energies of the various nuclei, we used the experimental mass excesses listed in the Möller and Nix tables (Möller *et al.* 1995).

The Level Density Parameter

At high energies, the level density parameter a behaves essentially as a function of mass number only. However, in cases where deformation and shell effects are important (often the case near closed neutron shells) it has been shown (Iljinov *et al.* 1992) that at low energies it is more appropriate to use an energy dependent form of the level density parameter;

$$a(U,Z,N) = \tilde{a}(A)\left[1 + \delta W(Z,N)\frac{f\left(U\right)}{U}\right] \quad (14)$$

with

$$f\left(U\right) = 1 - \exp\left(-\gamma U\right) \quad (15)$$

and as usual $U = E - \Delta$. In previous works where a more global prescription was developed [(Rauscher *et al.* 1997), (Iljinov *et al.* 1992)], one would adopt a semi-empirical shell correction, $\delta W\left(Z,N\right)$, and fit $\tilde{a}\left(A\right)$ to known experimental data. Here we choose to adopt a simple form for $\tilde{a}\left(A\right)$ and fit the shell correction.

In our analysis, we followed the convention of (Rauscher *et al.* 1997) in choosing the parameter $\gamma = 0.04884$ that describes the fall off in energy of the shell correction. We also chose a relatively simple form for the asymptotic value of the level density parameter, $\tilde{a}(A) = A/8$ (the fermi-gas result). It was discovered that in the energy range of interest to us, the exact form of $\tilde{a}(A)$ made very little difference in determining the shell corrections δW from experimental values of resonance spacings.

Shell Corrections

Shell corrections can be determined for select nuclei from experimental values of the average level spacings D_0 as determined by neutron resonance analysis (RIPL 1998). For $s-$wave resonances (neutron angular momentum equal to zero), the calculated level spacing, D_{calc}, evaluated at the neutron binding energy $U = B_n$, is related to the nuclear level density (e.g. Eq.'s [8-10])

$$D_{calc} = \frac{2}{\rho\left(U, J = \frac{1}{2}\right)} \quad (16)$$

for nuclei with $s = 0$ and

$$D_{calc} = \frac{2}{\rho\left(U, J = s + \frac{1}{2}\right) + \rho\left(U, J = s - \frac{1}{2}\right)} \quad (17)$$

for nuclei with $s \neq 0$. In each case, the level densities $\rho\left(U,J\right)$ were calculated using the other parameters $(\lambda, \Delta, \gamma, \tilde{a}(A))$ set as previously described. We then numerically solved for the value of δW that would minimize the quantity $D_{calc} - D_0$ using root bisection methods. This now completely describes the parameterization of σ^2 and $a(U,Z,N)$, and thus the Fermi-gas level density.

3.3.3. Systematic Behavior of Fermi Gas Level Density Parameters

There are only a limited number of nuclei for which the average resonance spacing D_0 has been measured (i.e. for compound nuclei formed from a stable target plus a neutron). As a result, we were required to systematically predict the shell correction for the remaining nuclei in the range of interest for this project. After plotting the experimental δW in our region of interest and their associated errors and adding 3 MeV to the odd-Z nuclei, we noted a roughly linear behavior. We made a χ^2 linear fit to the data, shown in figure 3. We then subtracted 3 MeV from the δW for odd-Z nuclei to account for the 3 MeV added prior to making the systematic. Of course, where available, we always used an experimentally determined shell correction over a systematic one.

3.3.4. Level Densities Below the Neutron Binding Energy

For the lower energy regions, below the neutron binding energy B_n, the nuclear level density has the same formulation as Eq. [8]. However, particularly at and below the pairing energy Δ, the state density in Eq. [9] becomes imaginary. Unfortunately, experimental level schemes are rarely known above 2 MeV of excitation energy. In practice we are forced again to assume a model and use

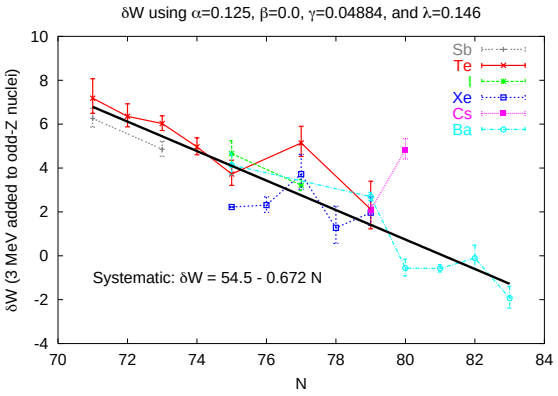

Fig. 3.— χ^2 linear fit to experimentally determined shell corrections, used to systematically determine unknown shell corrections.

all available experimental data to constrain its parameters.

Of course the two prescriptions for the level density must match at some energy intermediate to where they are constrained by experiment. Henceforth we will refer to the high energy level density as ρ_1, and the low energy density as ρ_2.

Gilbert and Cameron (Gilbert & Cameron 1965) noticed that the cumulative number of observed levels (the so-called staircase plot, which increase exponentially), can be fit with straight lines in a semi-log plot. They adopted a constant temperature formula to fit these:

$$N(E) = \exp\left[\frac{E - E_0}{T}\right] \tag{18}$$

with $N(E)$ being the cumulative number of levels at excitation energy E, E_0 and T are two free parameters to be fit to the observed level structure. The observable level density is given by

$$\rho_1(E) = \frac{dN(E)}{dE} = \frac{1}{T}\exp\left[\frac{E - E_0}{T}\right] \tag{19}$$

From classical thermodynamics, we have a definition of the nuclear temperature

$$\frac{d}{dE}\log\,\rho_1(E) = \frac{1}{T} \tag{20}$$

where T now takes on the meaning of a nuclear temperature which is constant in the region of the discrete levels. We assume that Eq. [18] can be extrapolated from the region of the known discrete levels to higher energies, where the Fermi-gas level density (ρ_1) is valid. We then define the notion of a fit to the total level density over the entire range as being achieved if: a) a good fit can be made to the low lying levels, b) the observed level spacing at the neutron binding energy is exactly reproduced, and c) the energy of the matching point E_x for the two prescriptions falls between $E = 0$ and $E = B_n$, and that they match at this point with the same slope, i.e. for $E = E_x$:

$$\rho_1(E_x) = \rho_2(E_x) \tag{21}$$

$$\frac{d\log\,\rho_1(E_x)}{dE} = \frac{d\log\,\rho_2(E_x)}{dE} \tag{22}$$

From the first of these, we can determine E_0:

$$E_0 = E_x - T\,\log\,T\rho_2\,(U_x) \tag{23}$$

where $U_x = E_x - \Delta$. The second condition can be satisfied by assuming that at E_x the constant nuclear temperature T of the low lying states is equal to the energy dependent nuclear temperature $\tau(U_x)$ of the high excited states,

$$\begin{aligned}\frac{1}{T} &= \sqrt{\frac{a}{U_x}} - \frac{3}{2U_x} \\ &+ \frac{(\tilde{a} - a)(1 + \gamma U_x) + \tilde{a}\gamma\delta W}{\sqrt{aU_x}}\end{aligned} \tag{24}$$

where a is given by Eq. [14]. If there is no shell correction, the latter term in the above equation is zero. Typical values for the matching energy are $2 \leq E_x \leq 5$ MeV, and are approximated by $E_x = 2.5 + \frac{150}{A} + \Delta$ (Gilbert & Cameron 1965). The constant temperature fits to the low lying levels of ^{127}I and ^{127}Xe is presented in Figure (4).

Behavior of the Spin Cutoff Parameter Below E_x

At the matching energy E_x, the spin cutoff parameter is given by Eq. [11]. Below this, we define E_{cut} as the energy of the highest known excited level for which energy, spin and parity are explicitly known and we calculate an analogous low energy spin cutoff parameter σ_L^2,

$$\begin{aligned}\sigma_H^2 &= \sigma_{E_x}^2 \\ U_L &= \max\left(E_{cut} - \Delta, 0.1\right)\end{aligned}$$

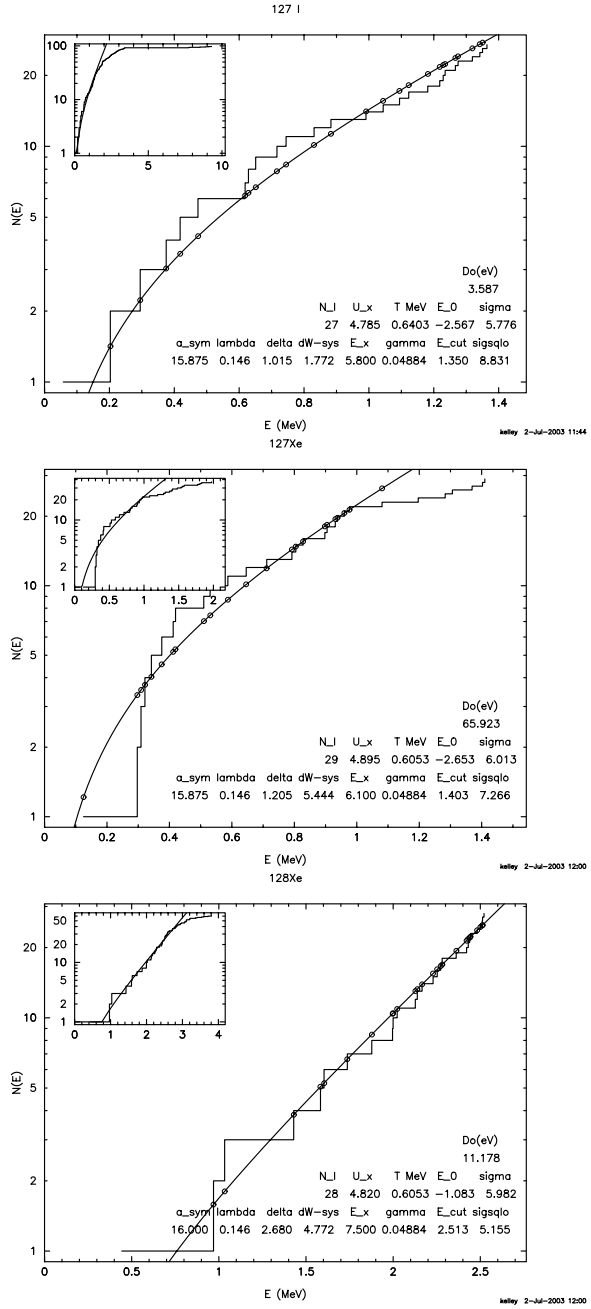

Fig. 4.— Constant temperature level density fits to the low lying spectroscopic levels of ^{127}I and ^{127,128}Xe.

$$\sigma_L^2 = \lambda\sqrt{aU_L}A^{2/3}$$
$$\sigma_G^2 = \sigma_L^2 + \frac{E - \frac{1}{2}E_{cut}}{E_x - \frac{1}{2}E_{cut}}(\sigma_H^2 - \sigma_L^2) \quad (25)$$

The form σ_G^2 is then used between $\frac{1}{2}E_{cut}$ and E_x.

The fitted parameters for the total level density are presented in Table 5 (Appendix A.5). The symbols in the legend are the same as described above. In column five, an "x" indicates the shell correction δW was derived from an experimentally known level spacing D_0, an "s" indicates the shell correction was derived from the systematic shown in Figure 3.

4. Calculated Cross Sections

4.1. Comparison to Measured Cross Sections

Having developed the various input quantities based on available experimental data in the previous section, we now turn to results of the STAPRE-H95 model and compare to available experimentally measured cross sections in the region of interest. Only results for targets initially in their ground states are available.

In Figure (5) we present the comparison for (n,γ), (n,2n), and (p,n) reactions on the target ^{127}I. These comprise the main destruction reactions for the loaded detector element iodine. Shown is the activation cross section (solid black lines in all plots that follow) defined as the sum of emission (both particle emission and gamma-ray cascade) from the compound nucleus that eventually leads to the ground state of the product (final) nucleus. We also provide (where appropriate) separate cross sections that decay to the ground state (red lines), and any long lived isomer (blue lines, see Table 2 (Appendix A.1) for a list of the isomers and their respective half-lives). These cross sections are plotted against the available experimental data, taken from the Experimental Nuclear Reaction Data File (CSISRS 2003). Cross sections for the total, ground, and isomeric states are colored the same as the modeled cross sections (black is activation, red is to ground, and blue to an isomer, respectively), with different symbols distinguishing results from various experiments.

For ^{127}I(n,γ)^{128}I, our result for the cross section is slightly low. At roughly 1 MeV the activation cross section is lower by ∼50%, but by 25 keV the difference is at most 5-10%. This is a good result for an (n,γ) activation cross section. Using global systematics, (n,γ) cross sections can typically be modeled within a factor of two, often to within

30% (Hoffman *et al.* 1999).

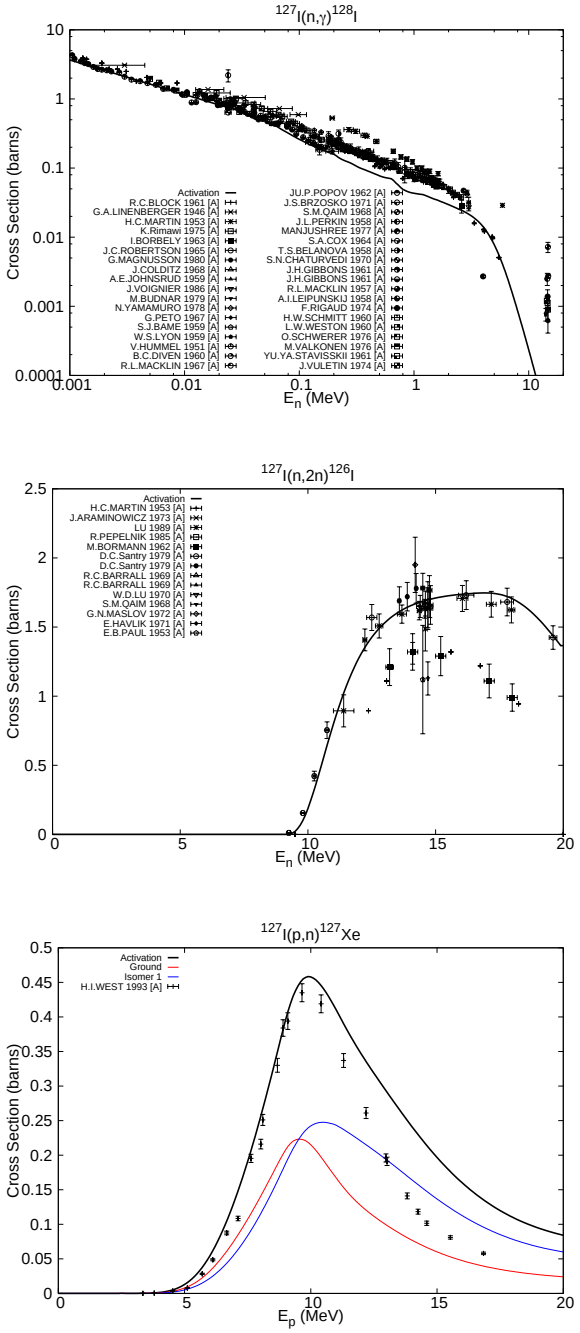

Fig. 5.— Calculated vs. experimental (n,γ), (n,2n), and (p,n) cross sections: ^{127}I.

With the exception of some older data sets, the ^{127}I(n,2n)^{126}I activation cross section shows good agreement with numerous experimental efforts. The most recent measurements seem to be in the best agreement, with our calculated cross section generally lying within the error bars. Predicting (n,2n) cross sections is fairly straightforward, as they scale roughly with the size of the nucleus, the activation cross section is typically 1-2 barns at 14 MeV regardless of atomic number in this region of the nuclear chart.

Finally, the ^{127}I(p,n)^{127}Xe cross section shows a very good shape over the entire excitation function, but above 10 MeV our cross section is higher than that measured by (West *et al.* 1993). The discrepancy is largest around 15 MeV, and is roughly 50%. For purposes of RADCHEM analysis, we use the measured cross sections in place of these modeled ones, although these results should be considered reasonable.

In our region of interest there are 29 other cross sections for which experimental data is available. Figures 22-23 (Appendix A.6) show (n,γ) cross sections that exhibit similar agreement (within $\sim$ 25%) to the ^{127}I capture reaction. The agreement was not quite as good for tellurium targets with an even number of neutrons, where our modeled cross section tended to be higher by as much as a factor of three.

It should be kept in mind that for comparisons to neutron induced experimental capture cross sections we are considering compound nuclear systems for which the important input parameters to our reaction model (e.g. those that affect level densities and photon-transmission coefficients) are often determined by normalization to experimental data (e.g. from resonance analysis), and so one would expect the comparisons to be good. Since these compound nuclei often bracket the systems of most interest to us, namely those which account for the dominant destruction reactions like (n,γ), our systematics should reasonably provide for similar agreement. It is therefore somewhat puzzeling that our results for Tellurium targets are consistantly high for even-even target nuclei. Direct reaction processes (not included here) would only make the disagreement larger. This merits further study.

Figures 27-28 (Appendix A.6) show (n,2n) cross sections that exhibit overall reasonable agreement (within $\sim$ 20%), similar to the ^{127}I(n,2n) activation cross sections. Finally, Figures 29-30 show the

available (n,p) and (p,xn) cross sections. The experimental data is often sparse and over a limited energy range, but the agreement is still reasonable. We note that (n,p) cross sections in this region are small (~ 10 mb).

4.2. Maxwellian Averaged Capture Cross Sections

Yet another comparison to experimental data comes from the extensive efforts to evaluate Maxwellian averaged capture cross sections for astrophysical applications (Bao *et al.* 2000). The Maxwellian-averaged neutron capture cross section is defined as the reaction rate $\langle \sigma v \rangle$ divided by the mean velocity $v_T = \sqrt{2kT/\mu}$ at a given temperature T. Here, μ is the reduced mass. For particle fluences and temperatures typical to stellar nucleosynthesis, the velocity distribution of the neutrons reduces to a Maxwell-Boltzmann distribution. In this case, the Maxwellian-averaged cross section reduces to (Beer *et al.* 1992)

$$\begin{aligned} \frac{\langle \sigma v \rangle}{v_T} &= \frac{\int_0^\infty \sigma_{n\gamma} v \Phi(v) dv}{v_T} \\ &= \frac{2}{\sqrt{\pi}(kT)^2} \int_0^\infty \sigma_{n\gamma}(E) W(E, kT) dE \end{aligned} \quad (26)$$

where $W(E, kT) = E \exp(-E/kT)$ and E is the center of mass energy.

Figures 24-26 (Appendix A.6) compare our calculated Maxwellian-averaged capture cross sections to experiment (Bao *et al.* 2000). The error bars on all points are identical and represent the measured error for a given cross section at 30 keV. We used spline interpolation to determine the value of the (n,γ) cross section between points on the energy grid. For energies below our lowest grid energy, we assume an (n,γ) cross section with an $E_{lab}^{-1/2}$ dependence. For energies greater than our highest grid energy, we take the cross section to be zero.

Overall our calculated maxwellian averaged cross sections agree with those of (Bao *et al.* 2000), with the most favorable comparisons for the iodine and xenon targets. Our results for the tellurium targets tend to be high, which is consistent with our comparison to other (n,γ) cross sections.

4.3. Sensitivity Studies

We illustrate the sensitivity of our modeled results to variations in the input parameters developed in §3 against the measured activation cross sections for (n,γ), (n,2n), and (p,n) on ^{127}I.

4.3.1. Sensitivity to the Pre-Equilibrium Cross Section

We adopt a simple exciton model with initial 2-particle 1-hole configuration. Average rates for internal transitions are related by the formulas of Williams (1970), corrected for the Pauli principle by Cline (1972), to the absolute square of the average effective matrix element $|M|$ of the residual interactions as per Eq. (7) of (Uhl & Strohmaier 1976). The dependence of $|M|^2$ on mass number and excitation energy is

$$|M|^2 = \langle FM \rangle A^{-3} E^{-1} \quad (27)$$

Figure (6) shows the sensitivity of the ^{127}I(p,n) and ^{127}I(n,2n) cross sections for variations of $50 \leq \langle FM \rangle \leq 200$. The variations affect the high energy tail of the (p,n) cross section, with a value of $\langle FM \rangle = 200$ providing the best agreement agreement with the experimental excitation function. This value also provided the best agreement with the (n,2n) experimental data. This value for $\langle FM \rangle$ was applied in calculating the pre-equilibrium contribution to all cross sections in this study.

4.3.2. Sensitivity to the choice of Level Density Prescription

The nuclear level density parameters developed for this region (Appendix A.5) reflect best choices from the available experimental data in the region of interest. Instead of varying each of the many parameters $(a(U, Z, N), \sigma^2, \lambda, \Delta, \delta_W)$, we instead present results where only the overall treatment of the level density prescription was varied, keeping all other parameter input fixed.

Figure (7) shows the experimental cross sections for (n,γ), (n,2n), and (p,n) cross sections on ^{127}I (for the sources of the experimental data, see Figure 5 and (CSISRS 2003)). For comparison we show our local systematic level density (red-solid line, Appendix A.5).

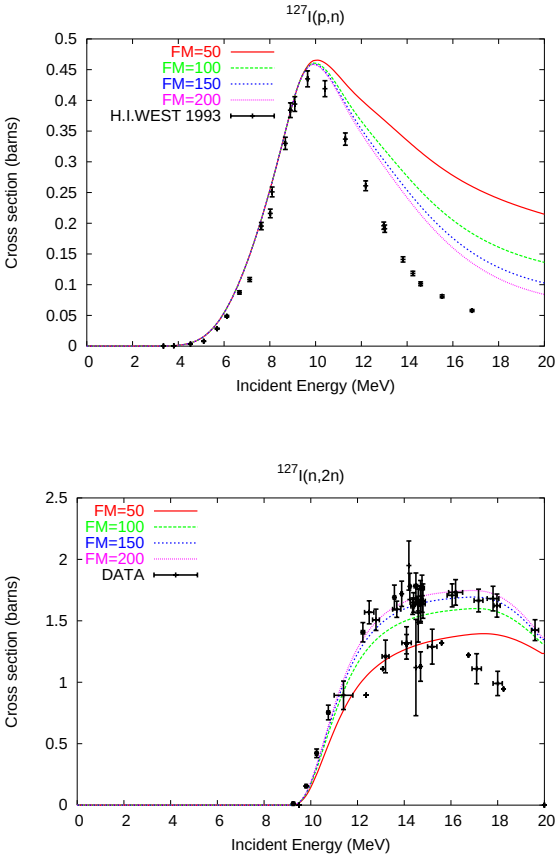

Fig. 6.— Sensitivity to pre-equilibrium matrix element.

The second level density prescription from (Rauscher *et al.* 1997) is plotted as the purple dashed line. This prescription is the current standard used in the calculation of cross sections for use in stellar nucleosynthesis calculations (Rauscher *et al.* 2002). This level density prescription is similar to ours, in that it also embodies an energy dependent $a(E)$ parameter (e.g. (Iljinov *et al.* 1992)) with shell corrections that damp out with increasing excitation energy (see our Eq. 14). This level density description differs from ours in the parameterization of the asymptotic value of the a parameter as well as the behaviour of the spin cutoff parameter at low energies (§3.3.4).

A third level density prescription is shown as the blue dotted line (Gilbert & Cameron 1965). This is one of the original prescriptions available and has been used to model some of the cross sections in the current RADCHEM sets (Vonach 1982). This prescription includes pairing and shell corrections but with an energy *independent* $a(A)$ parameter. It also served as the basis of the prescription used in the first large scale theoretical cross section library developed for use in modeling pre-supernova nucleosynthesis in stars [(Woosley *et al.* 1978), (Woosley & Weaver 1995)], and provided remarkable success in predicting measured solar abundances within the context of a study of Galactic Chemical Evolution (i.e. radchem for astrophysics). See (Timmes Woosley & Weaver 1995).

The last choice reflects a recent attempt to calculate level densities using microscopic nuclear structure models (Goriely 2002).

For the (n,γ) capture reaction, we see that three of the prescriptions (ours, Rauscher, and Goriely) all predict the same cross section below 1 MeV, and in good agreement with the experimental data below 200 keV. The Gilbert and Cameron level density results in a slightly larger cross section. All prescriptions indicate somewhat similar behavior above 1 MeV. Of course above 1 MeV the value of the cross section begins to drop rapidly ($\leq$ 10 mb), and so this would not compete with particle induced reactions for these higher energies. Overall, we believe our local systematic is in good agreement for the important energy range between 10 and 100 keV.

For the (n,2n) reaction we see that the three Fermi-Gas level densities all predict roughly the same cross section over the entire range of excitation energy studied. The microscopic level density of Goriely is lower by roughly 15% near 14 MeV. Again, we consider our local systematic to be preferable to any of the other three.

Finally, for the (p,n) cross section we see that all three Fermi gas level densities provide similar values for the peak of the (p,n) cross section, and differ from each other primarily in the high energy tail. The Goriely level density results in a peak which is significantly higher and occurring at a higher incident energy. Again, we consider our local systematic to do a good job on this cross section, recalling that we do use the actual measured cross section (West *et al.* 1993) in our RADCHEM calculations.

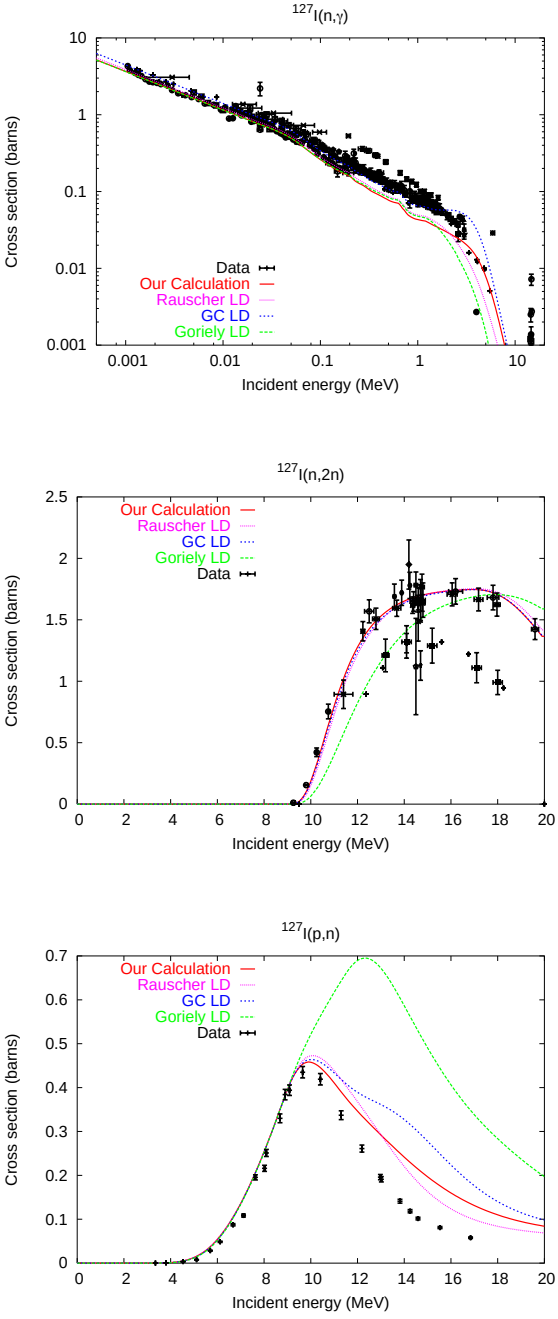

Fig. 7.— Sensitivity to the choice of level density prescription.

4.3.3. *Sensitivity to the Normalization of the γ-ray Transmission Coefficient*

Figure 8 shows the sensitivity to a ±30% change to the value of the average s-wave photon width used to normalize the gamma-ray transmission coefficients. The 30% variation translates into a nearly identical change in the cross section from 10 keV to 1 MeV. The (n,2n) and (p,n) cross sections do not exhibit any sensitivity because T_γ only entered into Eq. [1] in the denominator. In general, the smaller of the two transmission coefficients in the HF numerator will be the one that determines the cross section, especially if it is much smaller. This is always the case with photon vs. particle widths.

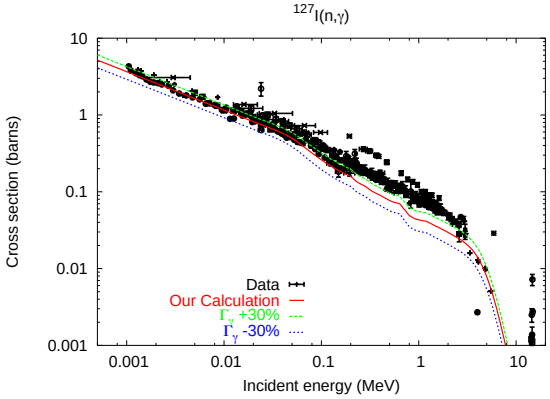

Fig. 8.— Sensitivity to a ±30% adjustment of the experimental s-wave average photon width.

4.3.4. *Sensitivity to the Inclusion of Width Fluctuation Corrections*

We adopt the Moldauer model of the WFC as embodied in the STAPRE code. For targets in the mass range of interest which have available experimental data, reaction thresholds are always greater than several MeV, and width fluctuation corrections will only be evident for capture reactions. Figure 9 shows the affect for the activation capture cross section of ^{127}I both with (solid red line) and without (green dashed line) WFC. The width fluctuation index (number of degrees of freedom) was two. As expected a decrease in the capture cross section is noticeable, although small (a few percent), below 500 keV. When the projectile energy increases, the capture cross section declines rapidly and the elastic enhancement vanishes. The (n,p) and (p,n) channels do not open until the incident neutron energy is above

2 MeV, and so no other channels can compete with the elastic and capture cross sections before the WFC are negligible. Nearly identical behavior is noted for neutron capture on ^{88}Sr and ^{93}Nb (Hilaire Lagrange & Koning 2003), see their Figures 2 and 3.

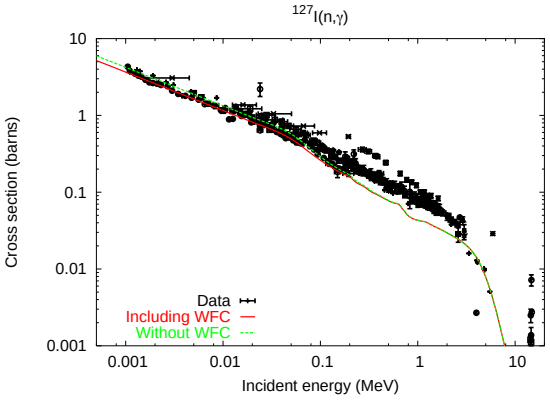

Fig. 9.— Sensitivity to inclusion or exclusion of width fluctuation corrections.

4.4. Production and Destruction Cross Sections

4.4.1. Results for ^{127}Xe

Figure 10 shows the modeled cross sections that directly affect the production and destruction of ^{127}Xe.

The modeled (p,n) production cross section is the only one of importance, since ^{127}I is the loaded isotope. Secondary pathways exist that proceed through other isotopes, but these would require that the intermediate radioactive isotopes be first populated though a series of (p,n) and (n,x) reactions from the loaded iodine isotope. The deuteron and triton induced cross sections were not modeled but taken from experiment (West *et al.* 1993). Of course the particle fluences play a dominant role in determining the most important cross sections. More specific details will be disclosed in the classified analysis presented in a following paper.

Of the destruction cross sections, the largest is ^{127}Xe(n,γ), becoming significant below ∼5 MeV of excitation energy. There is competition at intermediate energies between 4 and 7 MeV due to the (p,n) and (n,p) reactions on ^{127}Xe. It should be

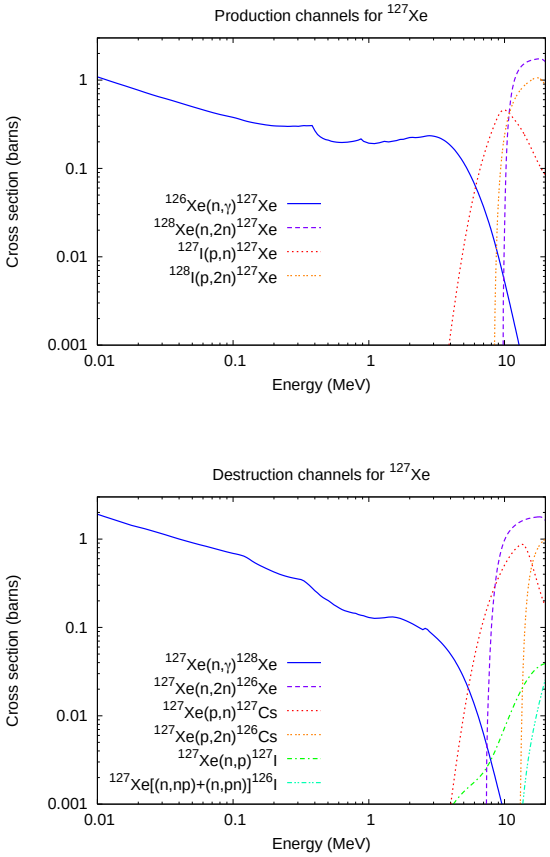

Fig. 10.— Calculated cross sections directly affecting production and destruction of ^{127}Xe.

noted that (n,p) cross sections were not included in the previous set (II0391). The impact of their inclusion on ^{127}Xe production will be investigated in the classified analysis.

The main model input parameter uncertainties for the ^{127}Xe(n,γ) cross section are the systematically determined values for the average photon width Γ_γ (§3.2.4), and the level density shell correction δW (§3.3.2) in the compound nucleus ^{128}Xe.

The upper left panel of Figure 2 (for even-Z even-N compound nuclei) shows that the fitted systematic is very nearly constant for $72 \leq N \leq 78$. The four data points represent Γ_γ values, from left to right, for the compound nuclear systems ^{123,125}Te+n and ^{129,131}Xe+n, respectively. The systematic predicts $\Gamma_\gamma = 130$ for N=74, almost ex-

actly the average value of the four measured photon widths, and within the error bar of the known Γ_γ for ^{125}Te+n (149 ± 45 meV). The average error bar reflects $\Delta\Gamma_\gamma = 25$ meV. This would translate into a roughly 20% uncertainty in the calculated ^{127}Xe capture cross section, although if one were to accept the central values, the error would be much less, $\sim 5 - 10\%$.

Figure 3 shows the fitted systematic to the shell correction δW. The plot shows significant scatter starting at $N = 75$, and for the Xe isotopes in general, exactly where we would like to have a tight fit. However, the Te isotopes show a remarkably linear behavior up to N=75, and are in very good agreement with the fitted systematic. We anticipate the error in the derived shell correction to be no more than 0.5 MeV, which could translate into a $\sim 15\%$ uncertainty in the capture cross section. Figure 11 shows this sensitivity as a percentage difference compared to our calculated cross section for the energy range $0 \leq E_n \leq 120$ keV.

The final item of possible uncertainty is the constant temperature level density fits for the nuclei involved in the ^{127}Xe(n,γ)^{128}Xe cross section. These are presented in Figure 4. The number of spectroscopic levels is good for all three participating nuclei and the fits are excellent.

Overall, the ^{127}Xe(n,γ)^{128}Xe cross section may be uncertain by roughly 15-25%. We note that our calculated Maxwellian capture cross section (Figure 25) for ^{126}Xe(n,γ)^{127}Xe was low by roughly 25%, while the ^{128}Xe(n,γ)^{129}Xe cross section was in excellent agreement. In particular, we note that the adoption of ^{127}I(n,γ) for ^{127}Xe(n,γ) that was done in the II0391 set was likely a poor choice, as these two capture cross sections differ by a factor of two to three over the energy range from $5 \leq E_n \leq 100$ keV (see Figure 12).

4.4.2. Results for Remaining Reactions in the Detector Set

In Figures 31-36 (Appendix A.7) we plot all modeled production and destruction cross sections for the elements Te, I, and Xe arranged by increasing neutron number. The variations on each cross section are often small, with the exception of two of the (n,p) cross sections (^{124}Te and ^{124}I). For these reactions Q_{np} becomes exoergic (Appendix A.3), and the low energy behavior of the cross section starts to assume a $1/\sqrt{E}$ behavior, as does (n,γ). In this mass range (n,p) reactions in a reaction network calculation can be ignored, since they are typically orders of magnitude smaller than cross sections of other neutron-induced reactions. There is a systematic reduction in the value of the capture cross section for targets with increasing neutron numbers. An odd-even effect is also evident, cross sections proceeding on odd-N targets are larger by roughly a factor of two over those proceeding on even-N targets over the mass range shown.

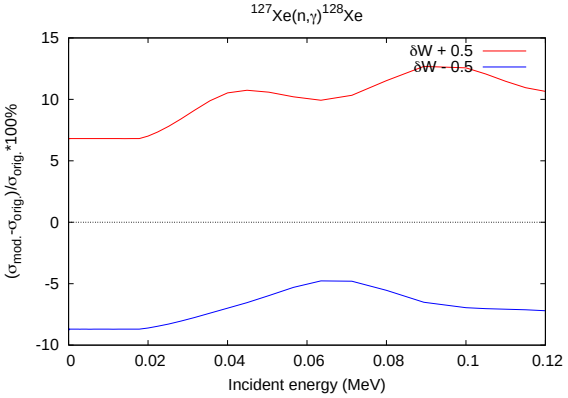

Fig. 11.— Sensitivity of the ^{127}Xe(n,γ) cross section to a ±0.5 MeV uncertainty in the shell correction used to normalize the Fermi-gas level density in ^{128}Xe.

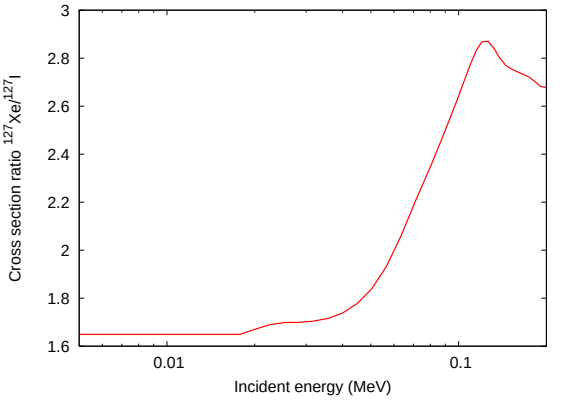

Fig. 12.— Ratio of calculated capture cross sections, ^{127}Xe(n,γ)/^{127}I(n,γ).

5. Conclusions

We have developed a new charged particle cross section set for radiochemical diagnostics of ^{127}Xe. The theory and implementation of the Hauser-Feshbach model were described, along with the details of the local systematics used to create a set of input parameters that reflect the latest available experimental data in the region of interest around ^{127}I. Sensitivity to the input models and parameters was explored. Overall we consider the modeling effort to be quite successful, in that our developed local systematics appear to well replicate measured cross sections over this restricted region of interest. Since we are interested in the production of one radioactive species, ^{127}Xe, the number of reactions that play a role in its activation are small. A similar case exists for another RADCHEM charged particle detector, ^{79}Br producing ^{79}Kr, for which a similar modeling effort has already been completed (Hoffman *et al.* 2004).

Improved confidence in this detector set could come when new techniques to measure cross sections on unstable targets are developed in the future. These are underway at LLNL using a surrogate reaction measurement method which is the subject of a current LDRD effort in N-Division (Escher *et al.* 2004). A proof of principle experiment to measure ^{85}Kr(n,γ)^{86}Kr is proposed for late 2005.

6. Acknowledgments

This work was performed under the auspices of the U.S. Department of Energy by the University of California Lawrence Livermore National Laboratory under contract W-7405-ENG-48.

REFERENCES

Avrigeanu, M. & Avrigeanu, V. IPNE-Bucharest Report No. NP-86-1995 (September 1995) http://www.nea.fr/abs/html/iaea0971.html

Bao, Z. Y., Beer, H., Käppeler, F.,, Voss, F., & Wisshak, K. 2000, Atomic Data & Nuclear Data Tables, **76**, 70

Bauer, R. 2002, private communication.

Beer, H., Voss, F., & Winters, R. R. 1992, ApJS, **80**, 403

Bohr, A., & Mottelson, B. *Nuclear Structure* Vol. 1, Single-Particle Motion, World Scientific, 1998

Experimental Nuclear Reaction Data File, Brookhaven National Laboratory, US Dept. of Energy, http://www.nndc.bnl.gov/nndc/exfor/

Chadwick, M. 1998, the GNASH statistical model code, http://www.nea.fr/abs/html/psr-0125.html

Cline, C. K. 1972, Nucl. Phys. **A195**, 353

ENSDF: Evaluated Nuclear Structure Data File, Brookhaven National Laboratory, US Dept. of Energy, http://www.nndc.bnl.gov/nndc/ensdf/

Escher, J., Ahle, L., Bernstein, L., Church, J.A., Dietrich, F., Forssen, C., and Hoffman, R. Surrogate nuclear reactions and the origin of the heavy elements, UCRL-PROC-205320

Gilbert, A., & Cameron, A.G.W. 1965, Can. J. Phys., **43**, 1446

Demetriou, P., & Goriely, S. 2001, Nucl. Phys. **A695**, 95

Hilaire, S., Lagrange, Ch., & Koning, A. J. 2003, Ann. of Phys. **306**, 209

Hofmann, H.M., Richert, J, Tepel, J. W. & Weidenmüller, H.A. 1975, Ann. of Phys. **90**, 403

Hoffman, R. D., Rauscher, T., Woosley, S. E. & Thielemann, F.-K. 1999, ApJ, **521**, 735

Hoffman, R.D., Dietrich, F.S., Bauer, R., Kelley, K., and Mustafa, M. 2004 UCRL-TR-205563

Iljinov, A.S., Mebel, M.V., Bianchi, N., De Sanctis, E., Guaraldo, C., Lucherini, V., Muccifora, V., Polli, E., Reolon, A.R., & Rossi, P. 1992, Nucl. Phys. **A543**, 517

Keisch, B. 1963, Phys. Rev. **129**, 769

Koning, A.J., & Delaroche, J.P. 2003, Nucl. Phys. **A713**, 231

Mclane, V., Dunford, C., & Rose, P. *Neutron Cross Sections*, Vol. 2, Neutron Cross Section Curves, Academic Press, 1988

Moldauer, P. A. 1976 Phys. Rev. **C14** 764

Möller, P., Nix, J.R., Myers, W.D., & Swiatecki, W.J. 1995, Atomic Data & Nuclear Data Tables, **59**, 185

Nethaway, D.R., Memo, "The Cross-Section Sets Used With the Watusi Program." LLNL A-Division memo, 5 Nov., 1998

Rauscher, T., Thielemann, F.-K., & Kratz, K.-L. 1997, Phys. Rev. C., **56**, 1613

Rauscher, T., Thielemann, F.-K. 2000, Atomic Data & Nuclear Data Tables, **79**, 47

Rauscher, T., Heger, A. Hoffman, R. D. & Woosley, S. E. 2002, ApJ, **576**, 323

Raynal, J. "ECIS96", Proceedings of the Specialists' Meeting on the Nucleon Nucleus Optical Model up to 200 MeV, 13-15 November 1996, Bruyeres-le-Chatel, Franc (http://www.nea.fr/html/science/om200/raynal.pdf)

Handbook for calculations of nuclear reaction data, Reference input parameter library. 1998, IAEA-TECDOC-1034 *http://www-nds.iaea.org/ripl/*

Timmes, F. X., Woosley, S. E., & Weaver, T. A. 1995, ApJS, **98** , 617

Woosley, S. E., Fowler, W. A., Holmes, J. A. & Zimmerman, B. A. 1978, Atomic Data & Nuclear Data Tables, **22**, 371

Woosley, S. E., & Weaver, T. A. 1995, ApJS, **101**, 181

Uhl, M., & Strohmaier, B. IRK-Vienna Report IRK-76/01 1976 (Upd. 1978)

Vonach, H. 1982, UCID-19549, LLNL

Walter, G. et. al. 1986, Nucl Sci. Eng., **93**, 357

West, H., Nuckolls, R., Hudson, B., Ruiz, B., Lanier, R., and Mustafa, M. 1993, Phys. Rev. C., **47**, 248

Williams, F. C. Jr. 1970, Phys. Lett. **31B**, 184

This 2-column preprint was prepared with the AAS LaTeX macros v5.0.

A. Basic Nuclear Structure Data

A.1. New Iodine Detector Set

^{A}Z	lifetime	(n,2n)	(n,n′)	(n,γ)	(n,p)	(n,np)	(p,n)	(p,2n)
^{121}Sb	57.21%	•		•			•	
^{123}Sb	42.79%	•		•			•	
^{123}Te	0.89%	•		•	•	•	•	•
^{123}Te$_m$	119.7 d	•	•	•	•	•	•	•
^{124}Te	4.74%	•		•	•	•	•	•
^{125}Te	7.07%	•		•	•	•	•	•
^{125}Te$_m$	57.40 d	•	•	•	•	•	•	•
^{126}Te	18.84%	•		•	•	•	•	•
^{127}Te	9.35 h	•		•	•	•	•	•
^{127}Te$_m$	109 d	•	•	•	•	•	•	•
^{128}Te	31.74%	•		•	•	•	•	•
^{124}I	4.1760 d	•		•	•	•	•	•
^{125}I	59.400 d	•		•	•	•	•	•
^{126}I	13.11 d	•		•	•	•	•	•
^{127}I	100%	•		•	•	•	•	•
^{128}I	24.99 m	•		•	•	•	•	•
^{129}I	1.57×10^7 y	•		•	•	•	•	•
^{125}Xe	16.9 h	•		•	•	•	•	•
^{125}Xe$_m$	56.9 s	•	•	•	•	•	•	•
^{126}Xe	0.089%	•		•	•	•	•	•
^{127}Xe	36.4 d	•		•	•	•	•	•
^{127}Xe$_m$	69.2 s	•		•	•	•	•	•
^{128}Xe	1.910%	•		•	•	•	•	•
^{129}Xe	26.40%	•		•	•	•	•	•
^{129}Xe$_m$	8.88 d	•	•	•	•	•	•	
^{130}Xe	4.071%	•		•	•	•	•	•
^{131}Xe	21.232%				•			
^{131}Xe$_m$	11.934 d				•			
^{133}Cs	100%	•		•	•			

Table 2: Cross sections: new iodine set.

A.2. Binding and Separation Energies

^{A}Z	J^{π}	BE (MeV)	S_n (MeV)	S_p(MeV)	S_α (MeV)	S_d (MeV)
^{121}Sb	5/2+	1026.32	6.81	8.01	1.67	12.71
^{123}Sb	7/2+	1042.10	6.47	8.59	2.19	12.94
^{123}Te	1/2+	1041.26	9.43	5.48	1.58	12.81
^{123}Te$_m$	11/2-					
^{124}Te	0+	1050.68	6.58	5.61	1.76	10.53
^{125}Te	1/2+	1057.26	9.11	6.18	2.09	13.09
^{125}Te$_m$	11/2-					
^{126}Te	0+	1066.37	6.29	6.21	2.23	10.81
^{127}Te	3/2+	1072.67	8.78	6.74	2.55	13.35
^{127}Te$_m$	11/2-					
^{128}Te	0+	1081.44	6.08	6.80	2.71	11.07
^{124}I	2-	1046.74	9.55	7.11	0.99	14.95
^{125}I	5/2+	1056.29	7.14	7.62	1.08	12.62
^{126}I	2-	1063.44	9.14	7.70	1.41	15.08
^{127}I	5/2+	1072.58	6.83	8.16	1.50	12.85
^{128}I	1+	1079.41	8.83	8.24	1.84	15.28
^{129}I	7/2+	1088.24	6.50	8.67	1.99	13.05
^{125}Xe	1/2+	1053.86	10.06	4.45	0.30	12.19
^{125}Xe$_m$	(9/2-)					
^{126}Xe	0+	1063.91	7.22	4.36	0.52	9.89
^{127}Xe	1/2+	1071.14	9.61	4.90	0.79	12.31
^{127}Xe$_m$	9/2-					
^{128}Xe	0+	1080.74	6.91	4.93	1.00	10.18
^{129}Xe	1/2+	1087.65	9.26	5.49	1.28	12.50
^{129}Xe$_m$	11/2-					
^{130}Xe	0+	1096.91	6.61	5.47	1.50	10.41
^{131}Xe	3/2+	1103.51	8.94	6.03	1.86	12.80
^{131}Xe$_m$	11/2-					
^{133}Cs	7/2+	1118.53	6.89	8.17	1.47	12.92

Table 3: Spins, parities, binding energies, and separation energies for new iodine set.

A.3. Q-values for Select Reactions

Target	(n,2n)	(n,p)	(n,np)	(p,n)	(p,2n)	(d,n)	(d,2n)
^{121}Sb	-9.24	0.39	-5.78	-1.82	-9.04	5.78	-4.04
^{123}Sb	-8.97	-0.62	-6.57	-0.84	-7.77	6.36	-3.06
^{123}Te	-6.93	0.84	-8.13	-2.02	-11.95	3.26	-4.24
^{124}Te	-9.43	-2.12	-8.59	-3.94	-11.44	3.38	-6.17
^{125}Te	-6.58	0.02	-8.70	-0.97	-10.52	3.95	-3.19
^{126}Te	-9.11	-2.89	-9.10	-2.94	-10.08	3.98	-5.16
^{127}Te	-6.29	-0.80	-9.19	-0.09	-9.23	4.52	-2.31
^{128}Te	-8.78	-3.60	-9.57	-2.03	-8.86	4.57	-4.26
^{124}I	-7.50	3.94	-5.48	-0.49	-10.96	4.89	-2.71
^{125}I	-9.55	0.97	-5.61	-2.43	-10.04	5.40	-4.66
^{126}I	-7.14	2.94	-6.18	0.48	-9.58	5.47	-1.75
^{127}I	-9.14	0.09	-6.21	-1.44	-8.67	5.94	-3.67
^{128}I	-6.83	2.03	-6.74	1.34	-8.27	6.02	-0.89
^{129}I	-8.83	-0.72	-6.80	-0.59	-7.50	6.44	-2.81
^{125}Xe	-7.60	2.43	-7.11	-3.88	-14.30	2.22	-6.11
^{126}Xe	-10.06	-0.48	-7.62	-5.61	-13.94	2.13	-7.83
^{127}Xe	-7.22	1.44	-7.70	-2.87	-12.83	2.67	-5.09
^{128}Xe	-9.61	-1.34	-8.16	-4.71	-12.47	2.71	-6.94
^{129}Xe	-6.91	0.59	-8.24	-1.98	-11.62	3.27	-4.20
^{130}Xe	-9.26	-2.17	-8.67	-3.76	-11.23	3.25	-5.99
^{131}Xe	-6.61	-0.19	-8.77	-1.13	-10.37	3.81	-3.36
^{133}Cs	-8.99	0.35	-6.08	-1.30	-8.49	5.94	-3.52

Table 4: Q-values (MeV) for select reactions in the new iodine set.

A.4. Adopted Level Schemes

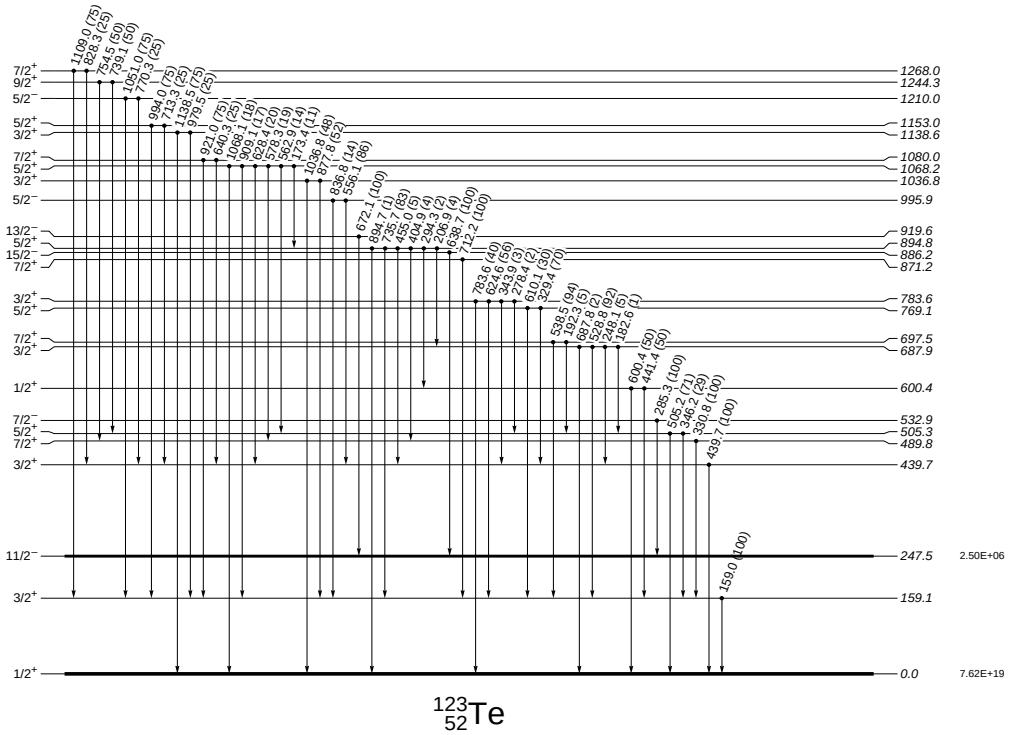

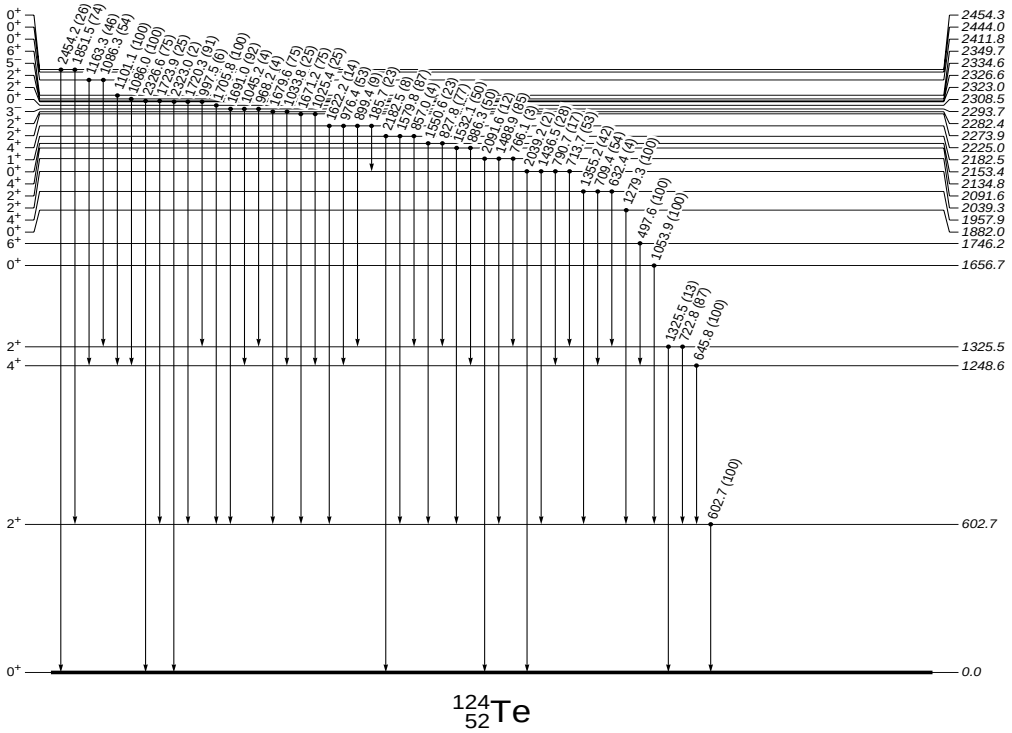

Fig. 13.— Adopted level schemes for ^{123,124}Te.

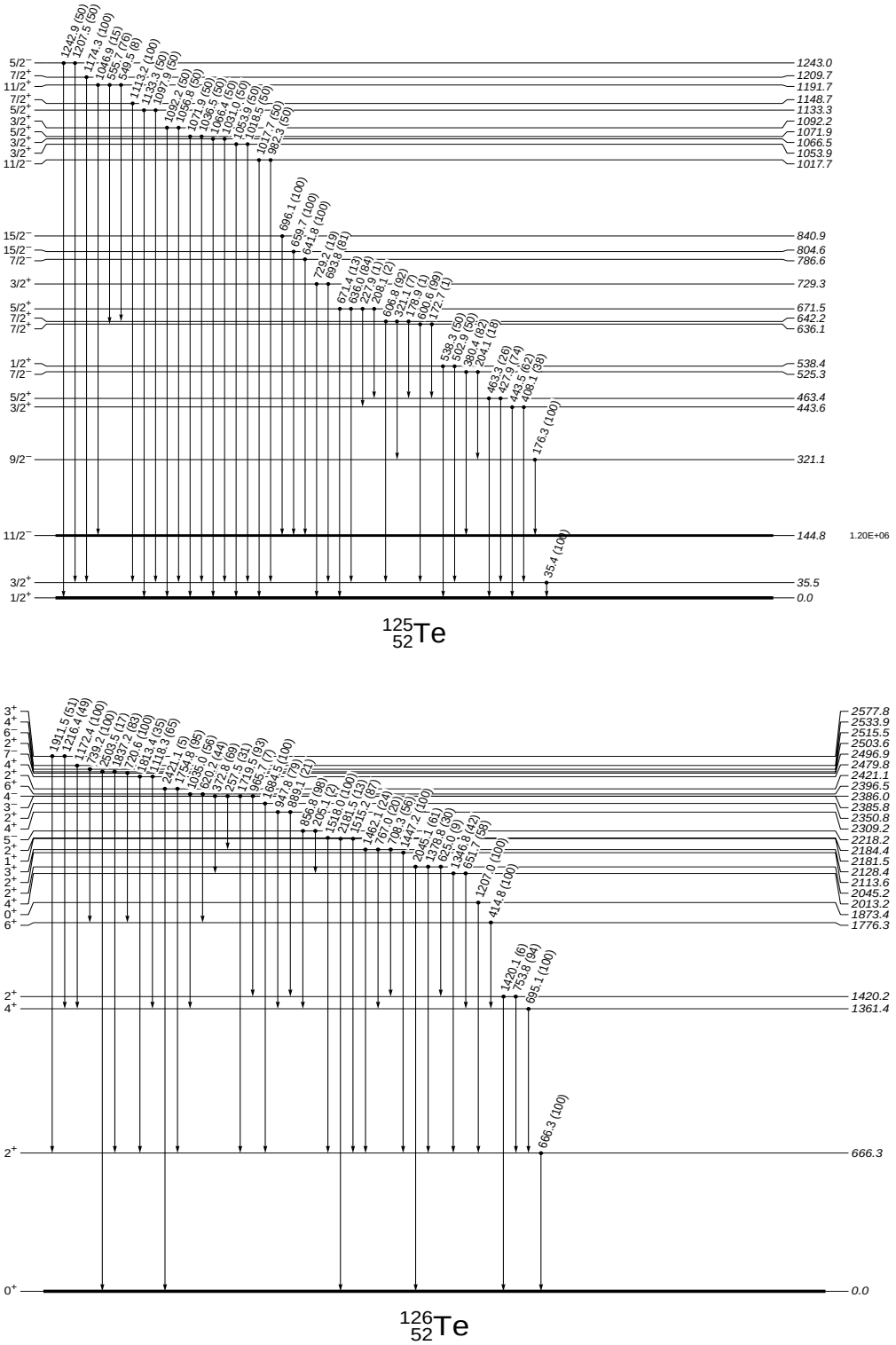

Fig. 14.— Adopted level schemes for ^{125,126}Te.

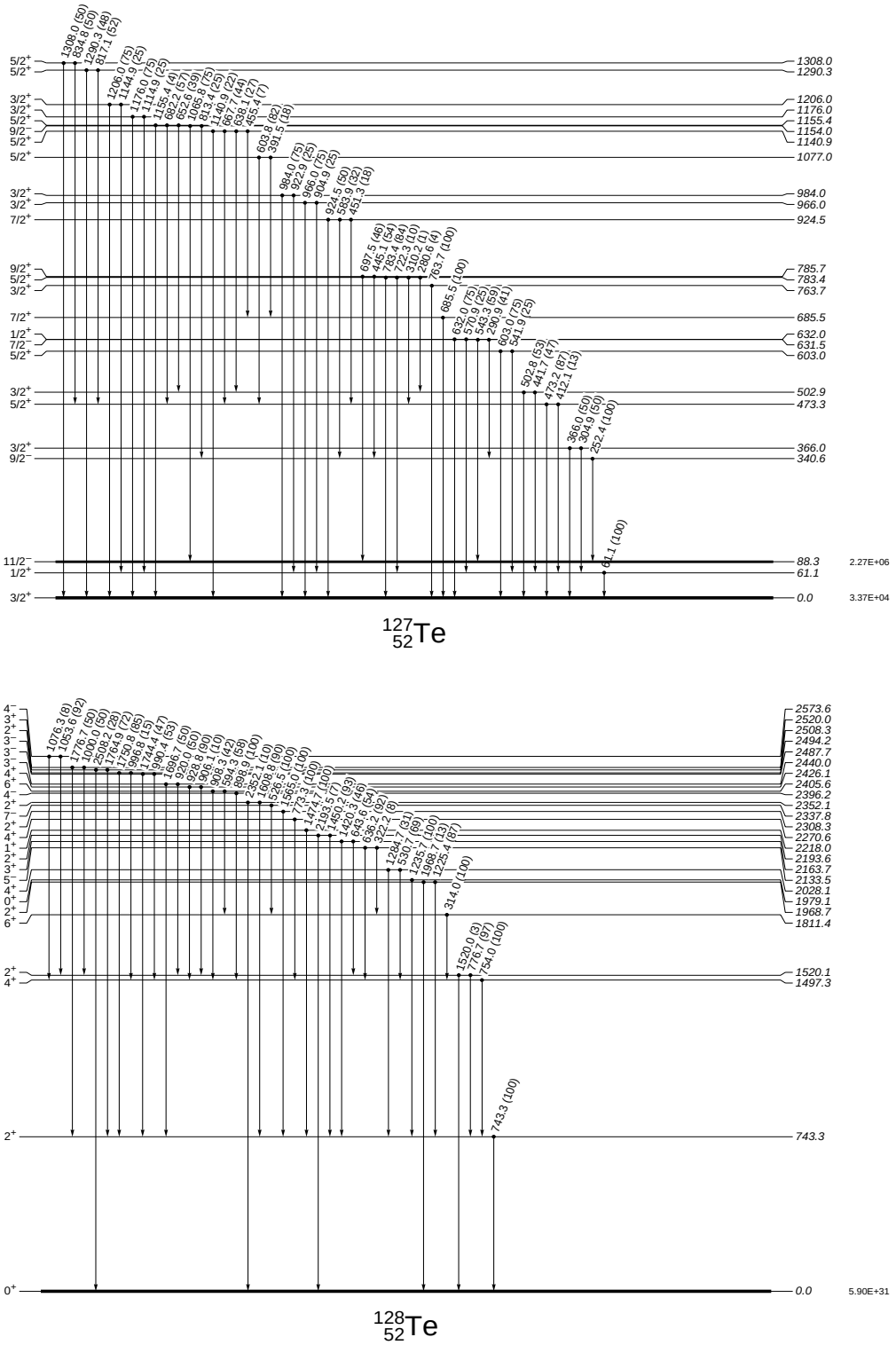

Fig. 15.— Adopted level schemes for ^{127,128}Te.

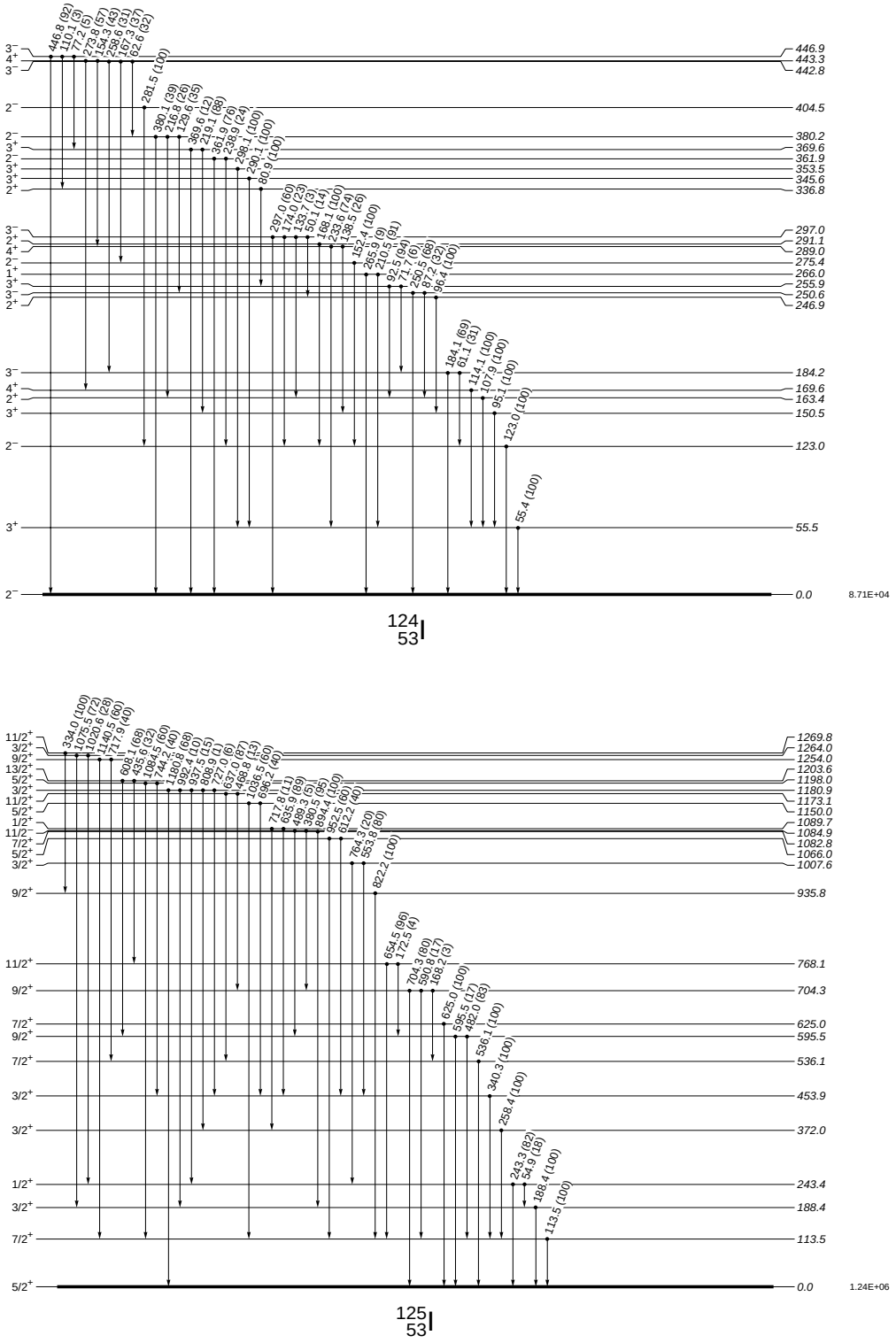

Fig. 16.— Adopted level schemes for ^{124,125}I.

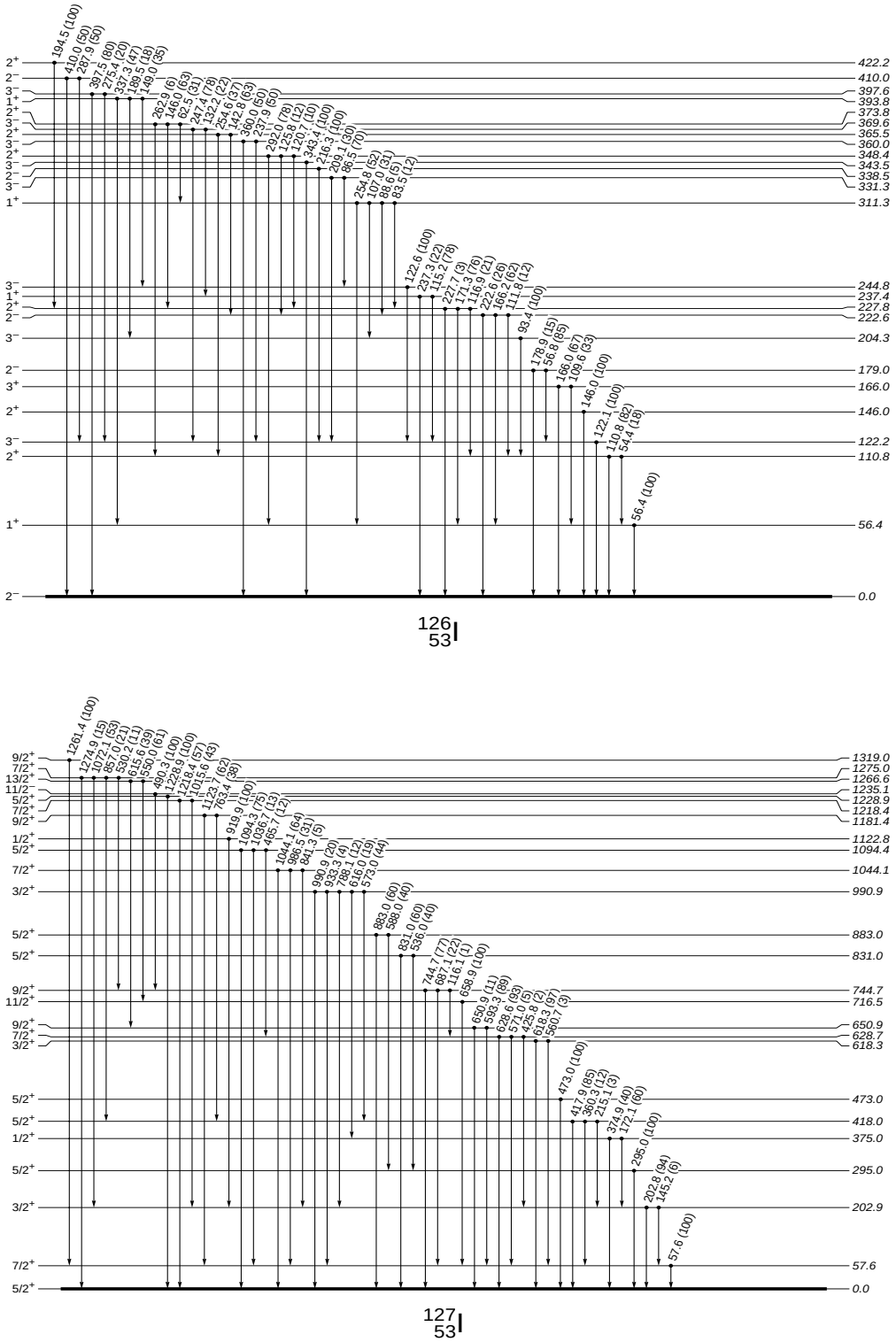

Fig. 17.— Adopted level schemes for ^{126,127}I.

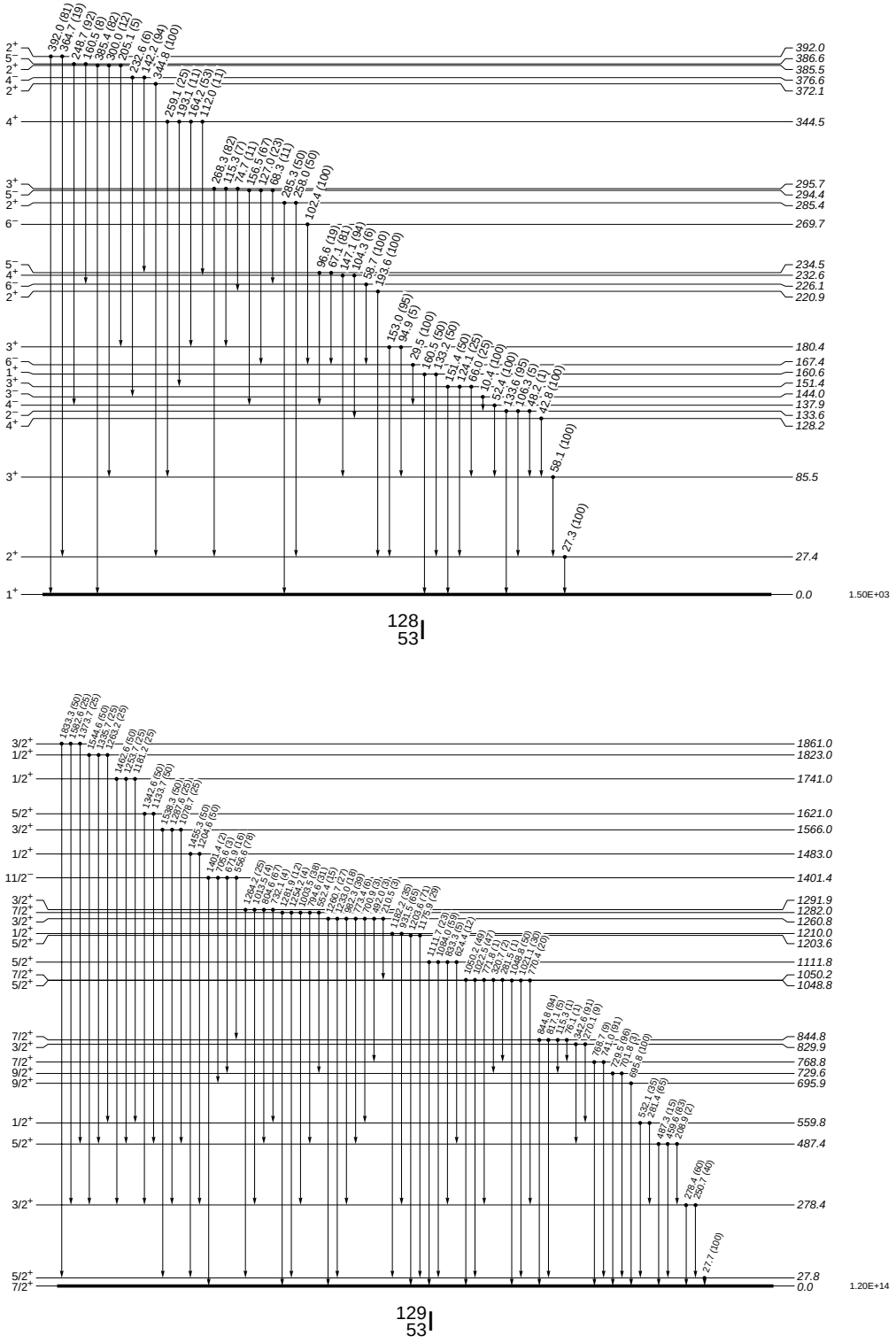

Fig. 18.— Adopted level schemes for ^{128,129}I.

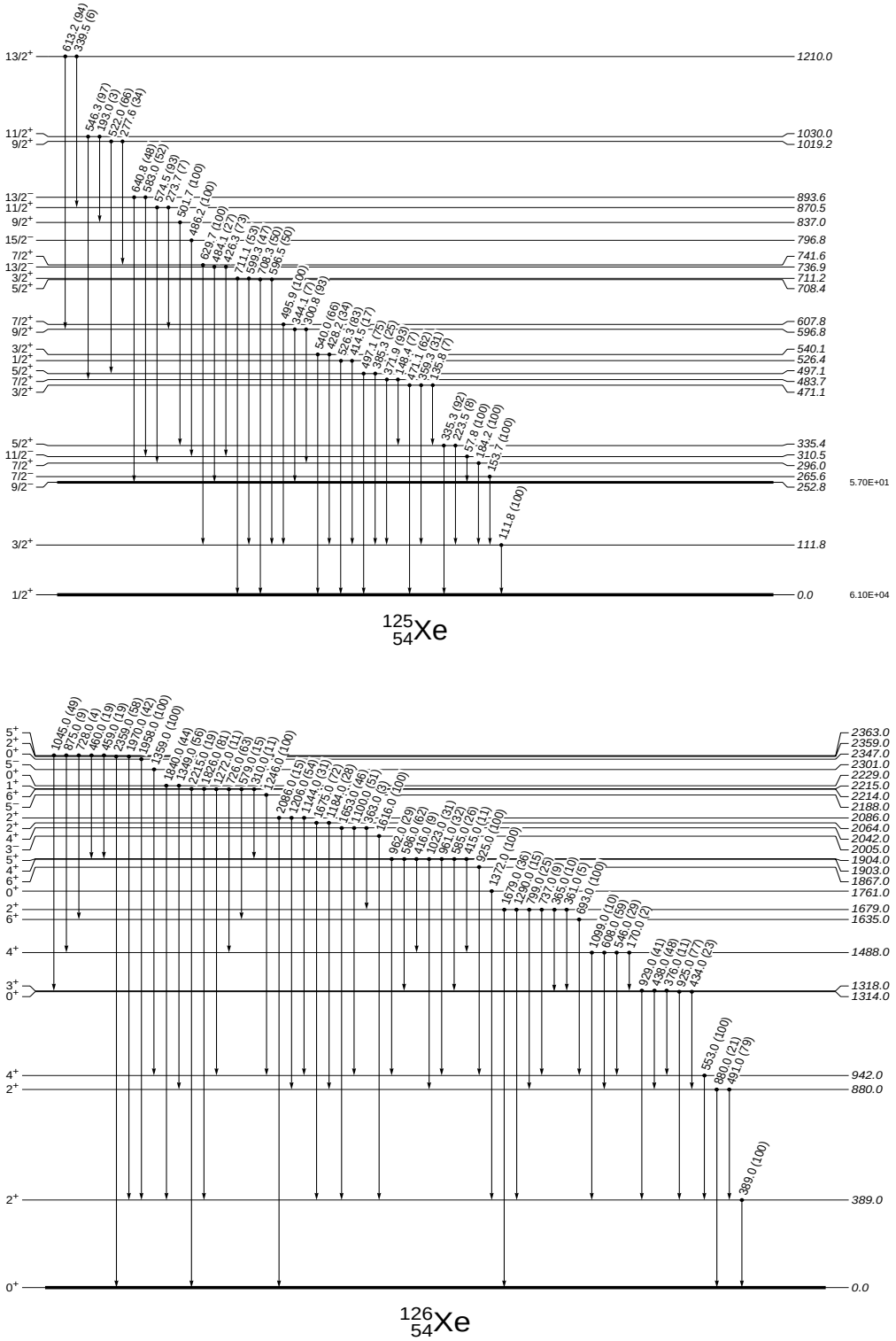

Fig. 19.— Adopted level schemes for ^{125,126}Xe.

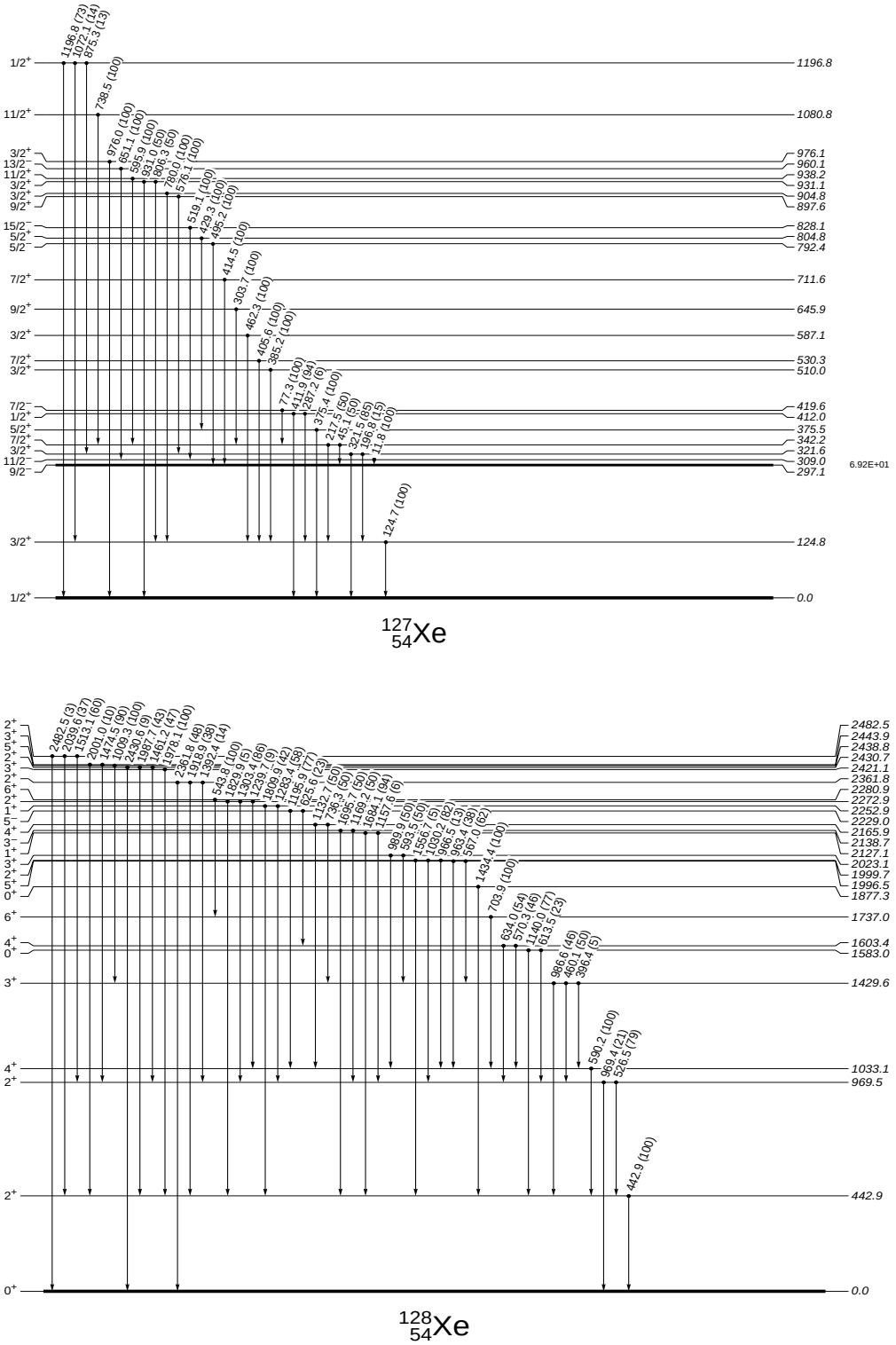

Fig. 20.— Adopted level schemes for ^{127,128}Xe.

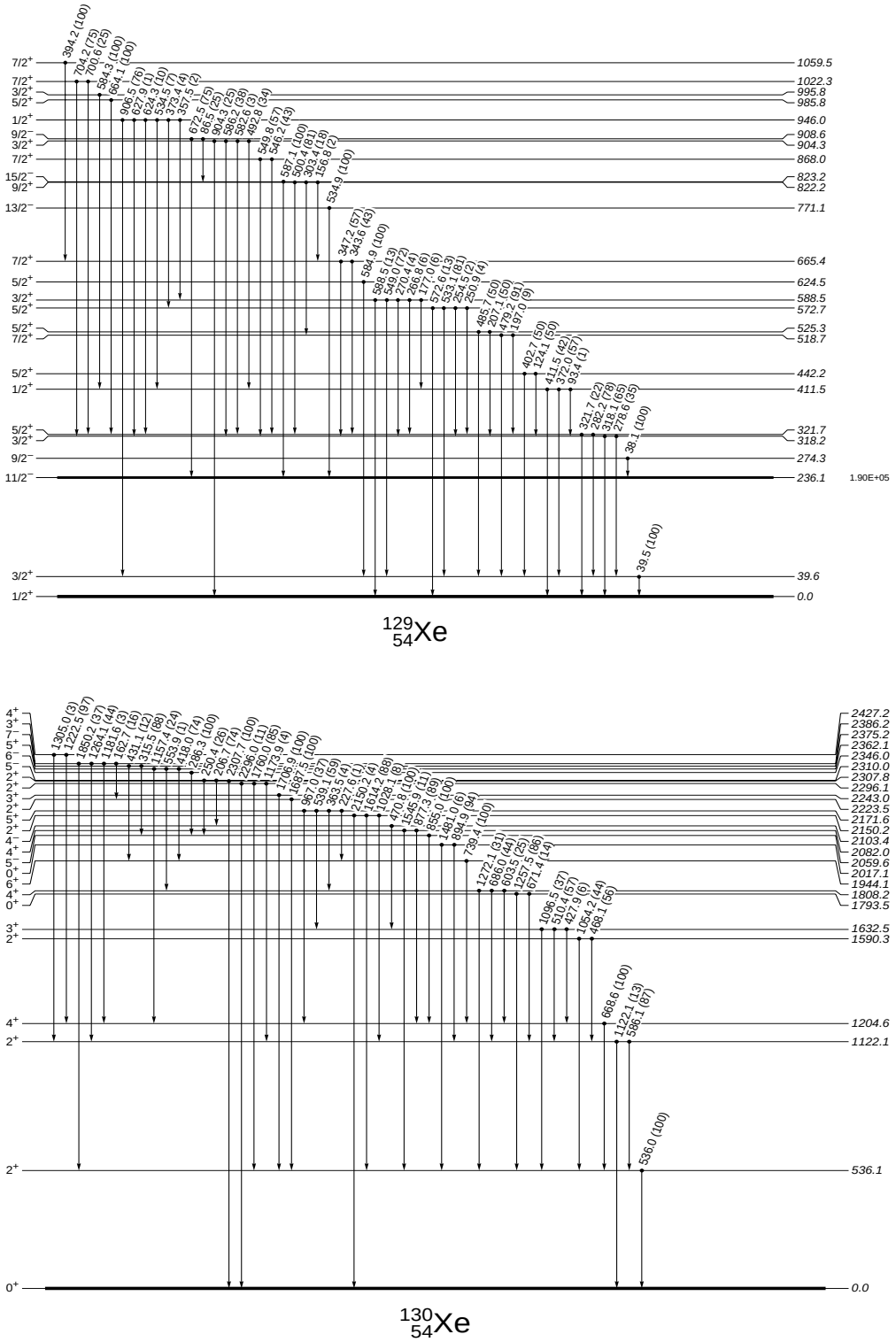

Fig. 21.— Adopted level schemes for ^{129,130}Xe.

A.5. Nuclear Level Density Parameters

^{A}Z	$\tilde{a}(A)$ (MeV)$^{-1}$	Δ (MeV)	δW (MeV)	x/s	$\sigma^2(E_x)$	E_x (MeV)	E_0 (MeV)	T (MeV)	N	E_{cut} (MeV)	$\sigma^2(E_{cut})$
^{121}Sb	15.125	1.130	4.460	s	5.247	4.400	-1.314	0.535	10	1.322	6.672
^{122}Sb	15.250	0.000	3.260	x	5.670	4.600	-3.496	0.627	7	0.167	6.126
^{123}Sb	15.375	1.120	3.116	s	5.193	4.300	-1.223	0.539	7	1.181	4.783
^{124}Sb	15.500	0.000	1.854	x	5.901	5.500	-4.165	0.687	14	0.287	7.957
^{125}Sb	15.625	1.180	1.772	s	5.147	4.300	-1.085	0.546	9	1.484	8.270
^{126}Sb	15.750	0.000	1.100	s	5.802	5.100	-3.794	0.669	6	0.128	5.330
^{127}Sb	15.875	1.200	0.428	s	4.983	4.000	-0.795	0.536	3	0.778	4.693
^{128}Sb	16.000	0.000	-0.244	s	5.935	5.700	-4.174	0.711	6	0.128	5.277
^{122}Te	15.250	2.840	7.460	s	5.904	7.500	-0.882	0.586	28	2.690	5.107
^{123}Te	15.375	1.265	7.180	x	5.782	5.500	-2.071	0.562	32	1.484	7.604
^{124}Te	15.500	2.995	6.354	x	5.980	7.900	-0.906	0.605	22	2.350	5.106
^{125}Te	15.625	1.310	6.025	x	5.926	6.000	-2.388	0.594	25	1.243	5.127
^{126}Te	15.750	3.025	4.964	x	5.954	7.900	-0.791	0.612	26	2.585	5.078
^{127}Te	15.875	1.335	3.726	x	5.935	6.280	-2.483	0.626	25	1.308	5.009
^{128}Te	16.000	3.045	3.428	s	6.035	8.300	-1.023	0.643	25	2.574	5.025
^{129}Te	16.125	1.675	5.141	x	6.149	6.900	-2.463	0.621	26	1.558	5.232
^{123}I	15.375	1.070	4.460	s	5.709	5.500	-2.337	0.601	28	1.391	8.770
^{124}I	15.500	0.000	3.788	s	5.722	4.500	-3.440	0.610	25	0.447	10.318
^{125}I	15.625	1.045	3.116	s	5.729	5.600	-2.412	0.617	25	1.270	7.294
^{126}I	15.750	0.000	2.444	s	5.823	4.900	-3.711	0.642	25	0.422	9.952
^{127}I	15.875	1.015	1.772	s	5.776	5.800	-2.567	0.640	27	1.350	8.831
^{128}I	16.000	0.000	1.659	x	5.973	5.400	-4.078	0.672	27	0.426	10.024
^{129}I	16.125	1.060	0.428	s	5.674	5.600	-2.256	0.638	25	1.861	13.521
^{130}I	16.250	0.000	0.216	x	6.219	6.499	-4.855	0.738	30	0.378	9.332
^{124}Xe	15.500	2.735	7.460	s	6.023	7.600	-1.176	0.592	22	2.676	5.201
^{125}Xe	15.625	1.330	6.788	s	6.108	6.500	-2.831	0.613	28	1.316	5.188
^{126}Xe	15.750	2.690	6.116	s	5.995	7.500	-1.120	0.597	28	2.455	5.182
^{127}Xe	15.875	1.205	5.444	s	6.013	6.100	-2.653	0.605	29	1.403	7.266
^{128}Xe	16.000	2.680	4.772	s	5.982	7.500	-1.083	0.605	28	2.513	5.155
^{129}Xe	16.125	1.140	2.223	x	6.050	6.600	-3.028	0.665	32	1.762	12.355
^{130}Xe	16.250	2.670	2.310	x	5.960	7.700	-1.148	0.638	26	2.442	5.009
^{131}Xe	16.375	1.240	3.722	x	5.987	6.000	-2.428	0.605	12	0.806	5.195
^{132}Xe	16.500	2.840	1.276	x	5.960	7.900	-0.945	0.646	5	1.804	4.994
^{125}Cs	15.625	0.865	4.460	s	5.827	5.500	-2.720	0.607	30	2.699	21.360
^{126}Cs	15.750	0.000	3.788	s	5.226	3.000	-2.218	0.512	5	0.258	8.002
^{127}Cs	15.875	0.950	3.116	s	5.932	6.000	-2.925	0.639	8	0.454	4.951
^{128}Cs	16.000	0.000	2.444	s	5.204	3.000	-2.191	0.522	1	0.000	4.944
^{129}Cs	16.125	0.950	1.772	s	5.965	6.200	-3.015	0.659	7	0.426	4.911
^{130}Cs	16.250	0.000	1.100	s	5.438	3.654	-2.659	0.574	1	0.000	4.892
^{131}Cs	16.375	0.940	0.428	s	5.994	6.400	-3.105	0.681	8	0.585	4.863
^{132}Cs	16.500	0.000	-0.244	s	5.758	4.700	-3.406	0.647	6	0.186	6.595
^{133}Cs	16.625	0.995	-0.916	s	5.860	6.100	-2.677	0.674	8	0.706	4.807

Table 5: Level density parameters calculated for new iodine set.

A.6. Modeled Cross Sections vs. Experiment

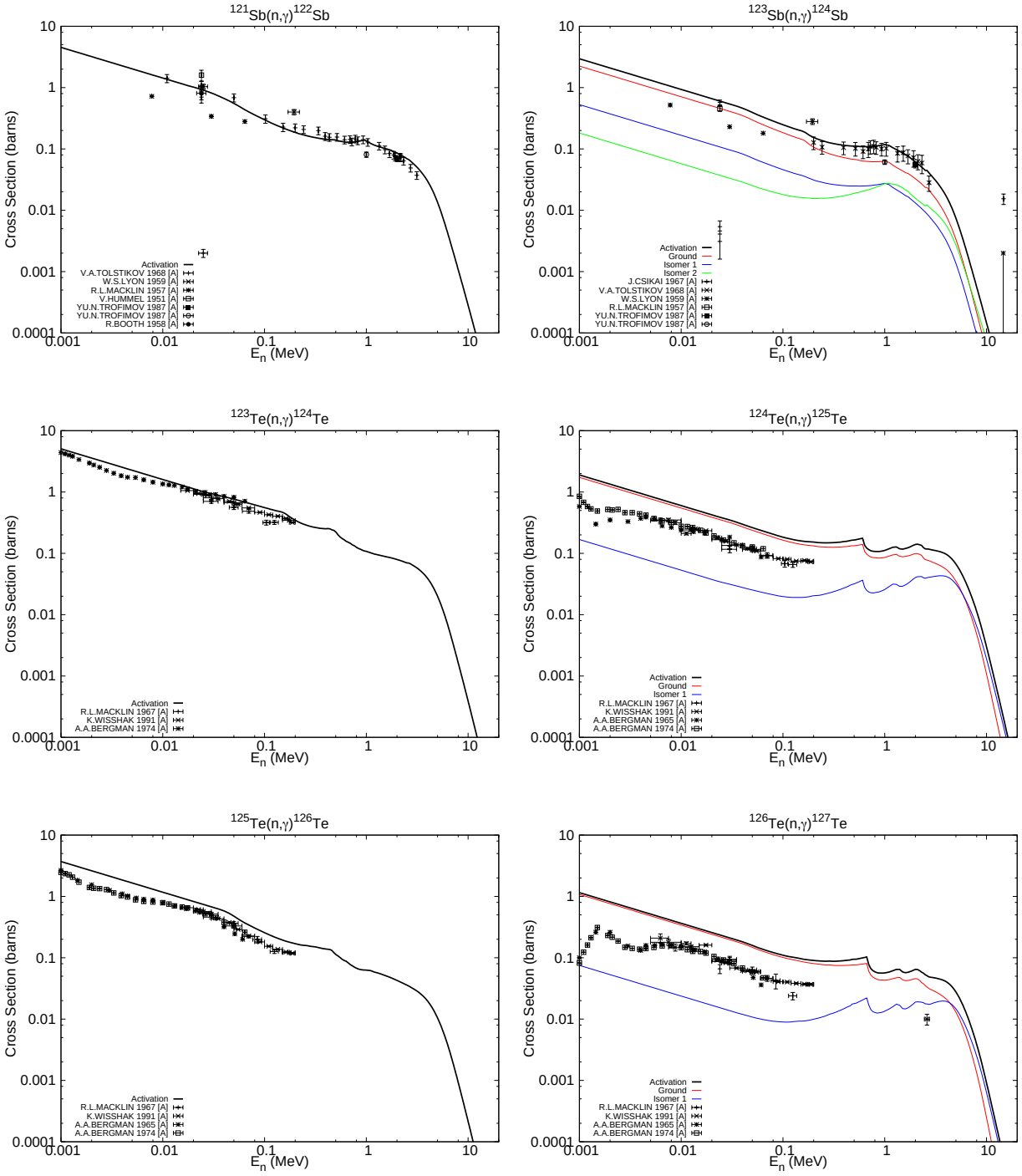

Fig. 22.— Measured vs. calculated (n,γ) cross sections on Sb and Te targets.

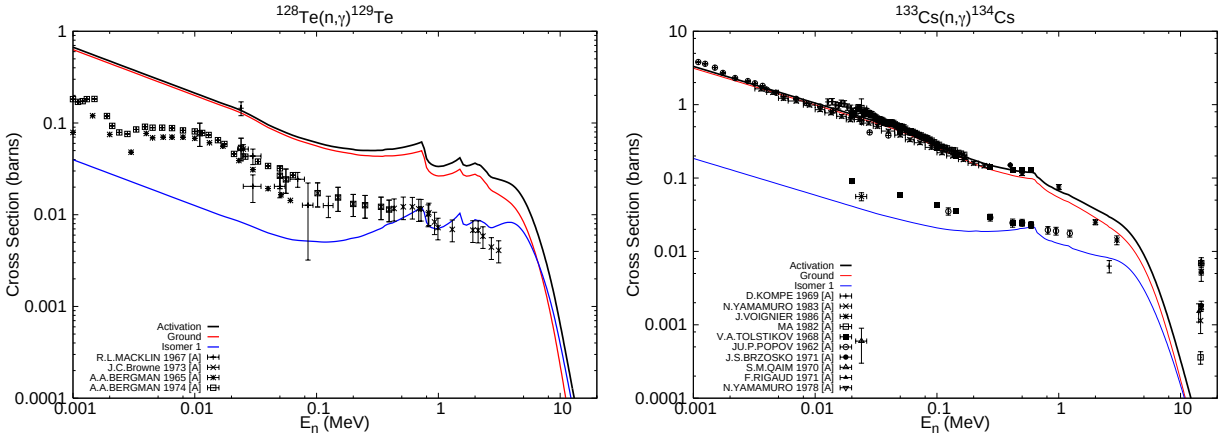

Fig. 23.— Measured vs. calculated (n,γ) cross sections on Te and Cs targets.

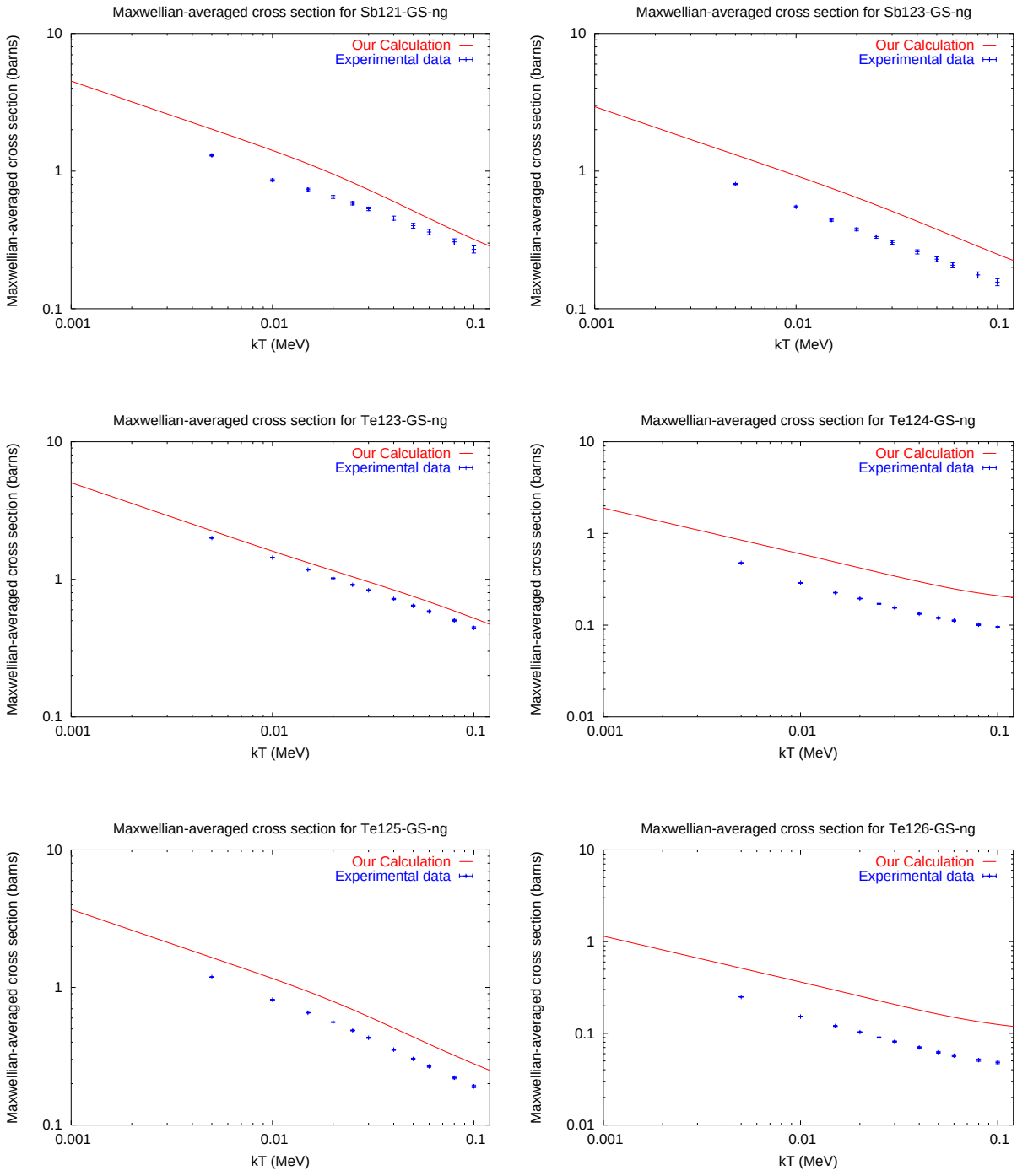

Fig. 24.— Measured vs. calculated maxwellian averaged (n,γ) cross sections for ^{121,123}Sb, and $^{123-126}$Te targets.

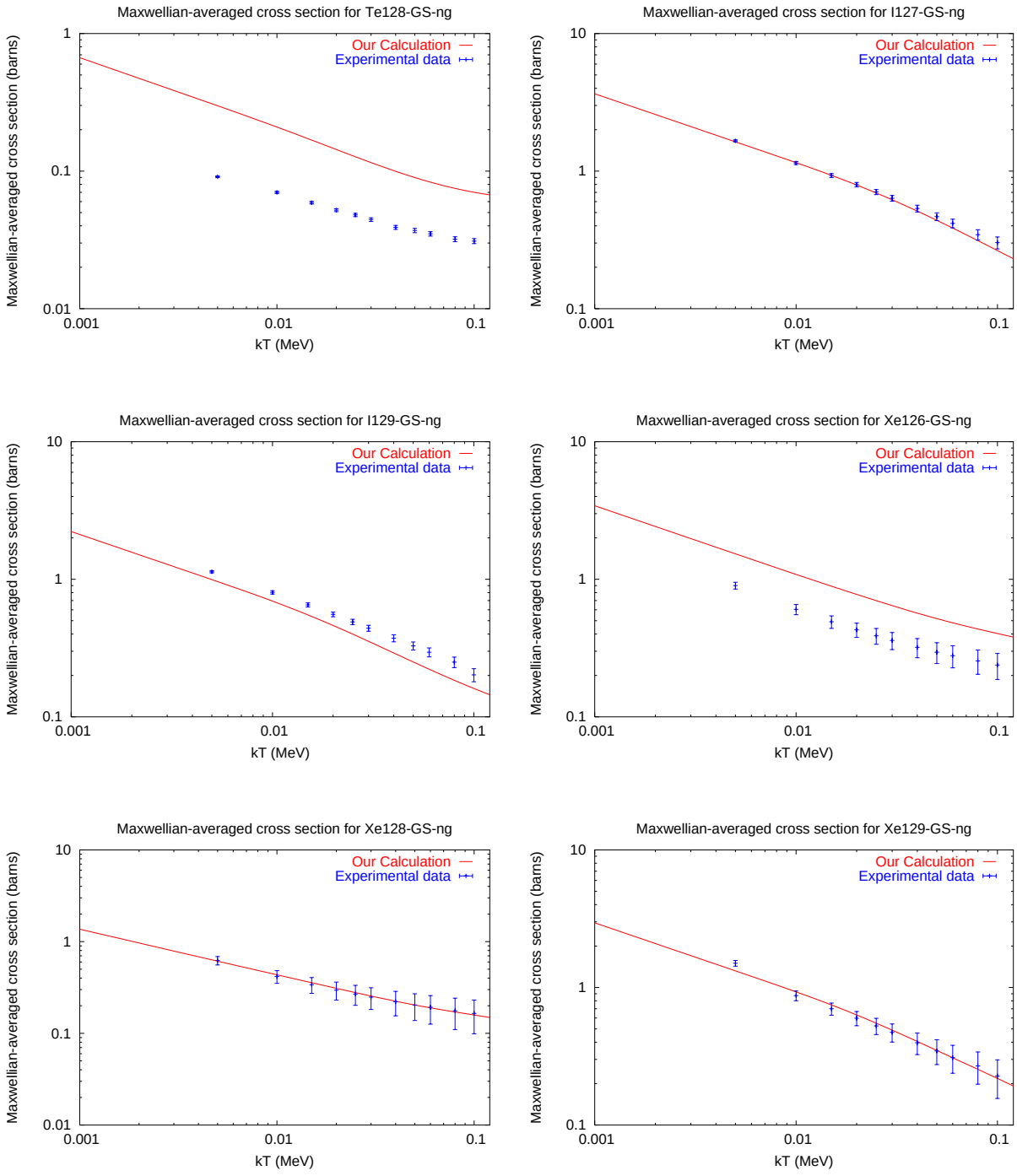

Fig. 25.— Measured vs. calculated maxwellian averaged (n,γ) cross sections for ^{128}Te, ^{127,129}I, and ^{126,128,129}Xe targets.

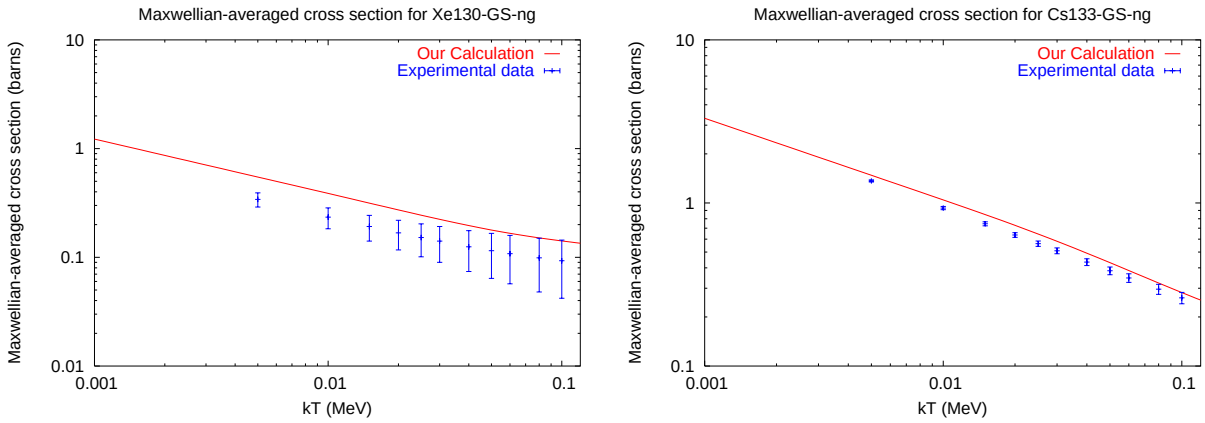

Fig. 26.— Measured vs. calculated maxwellian averaged (n,γ) cross sections on ^{130}Xe and ^{133}Cs targets.

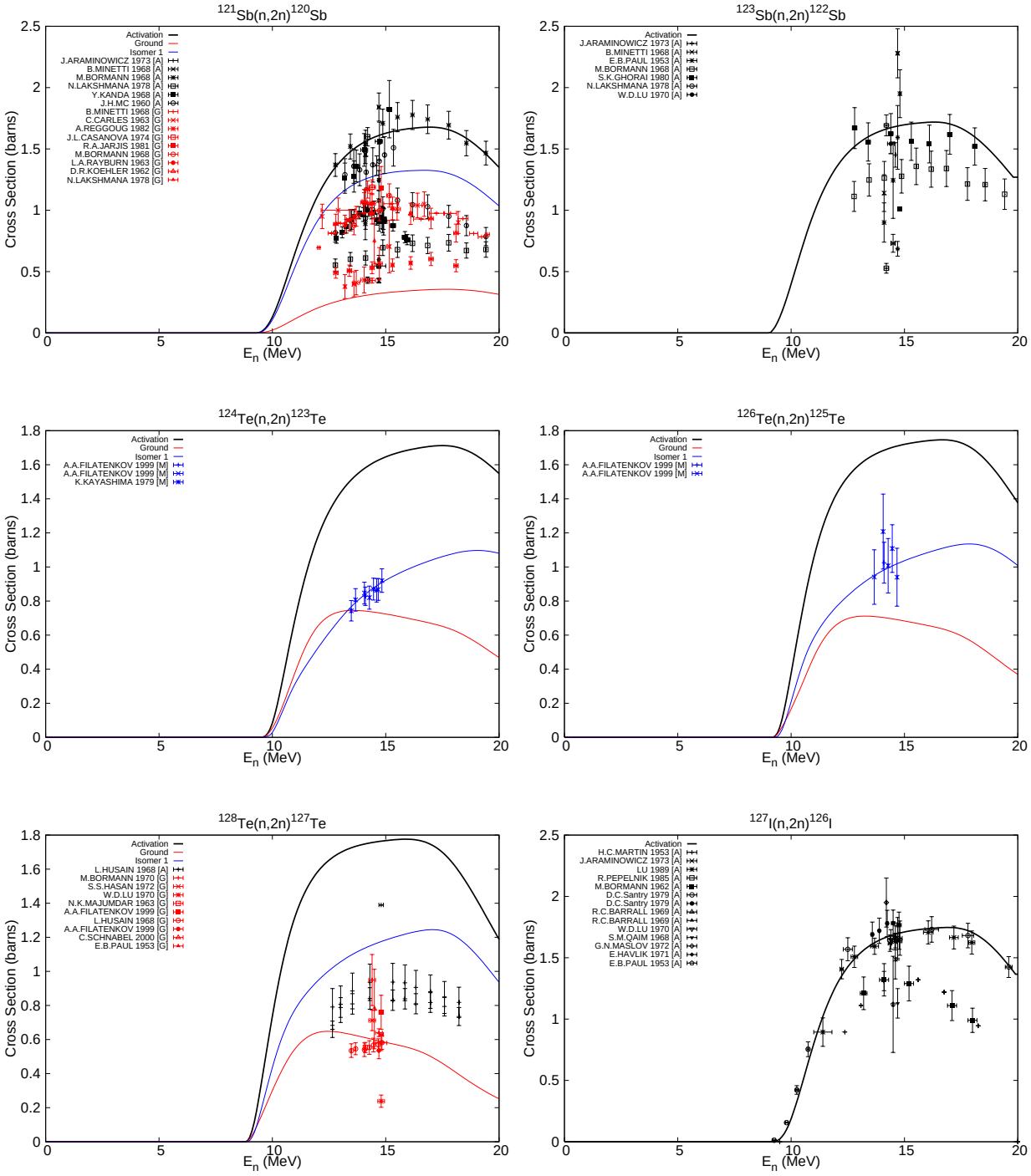

Fig. 27.— Measured vs. calculated cross sections for (n,2n) reactions on Sb, Te, and I targets.

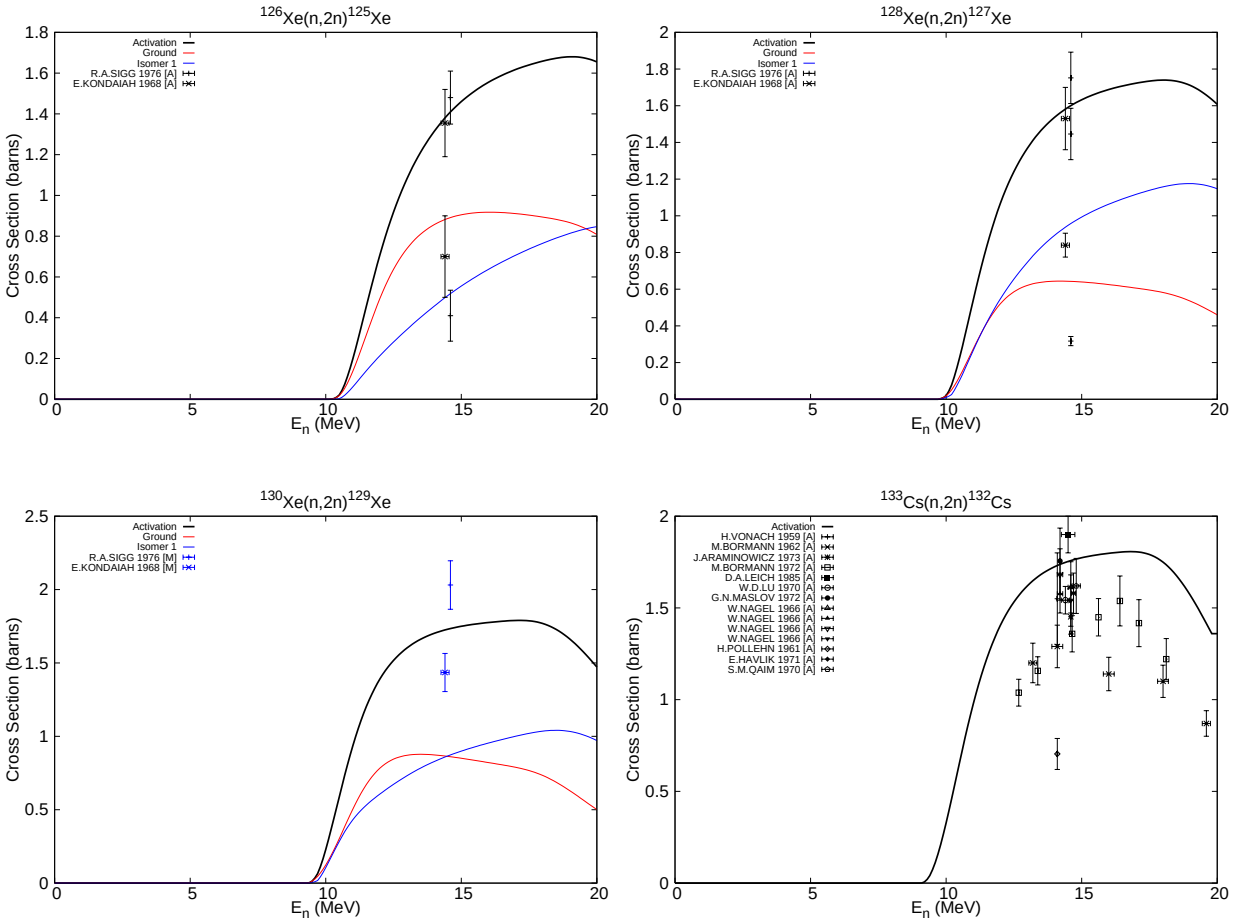

Fig. 28.— Measured vs. calculated cross sections for (n,2n) reactions on Xe and Cs targets.

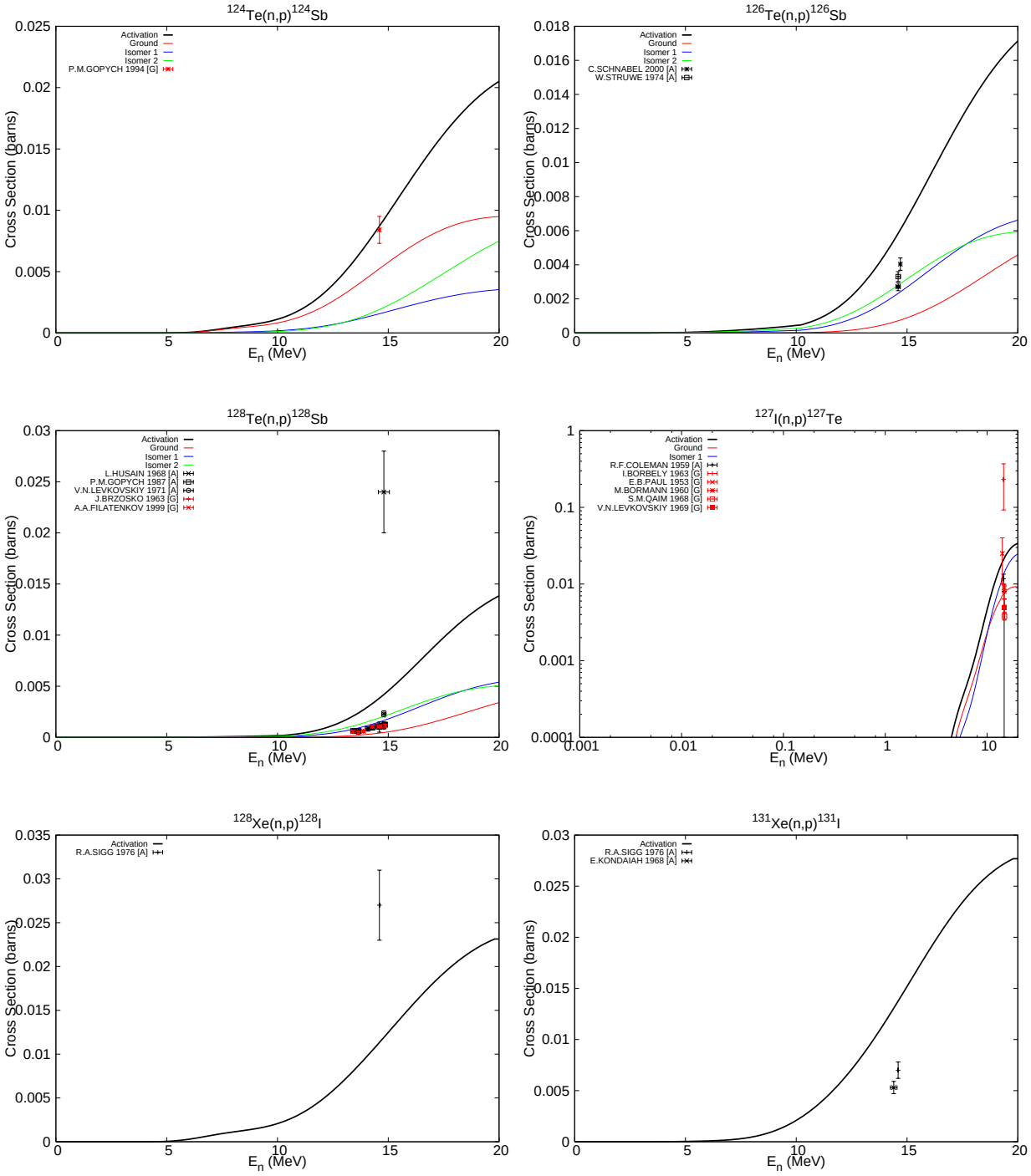

Fig. 29.— Measured vs. calculated cross sections for (n,p) reactions on Te, I, and Xe targets.

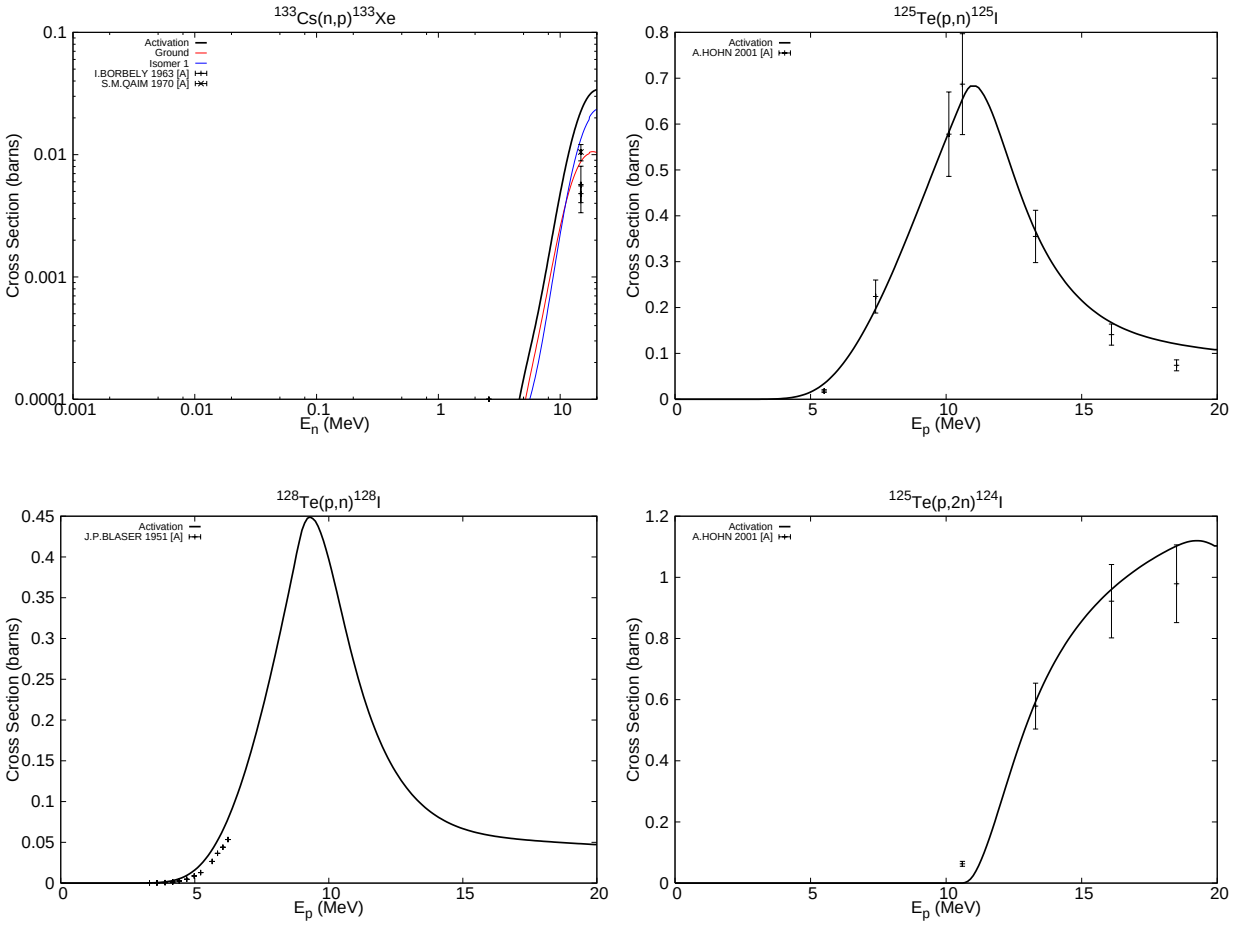

Fig. 30.— Measured vs. calculated cross sections for (n,p) and (p,xn) reactions on Cs and Te targets.

A.7. Modeled Cross Sections: Production and Destruction Channels

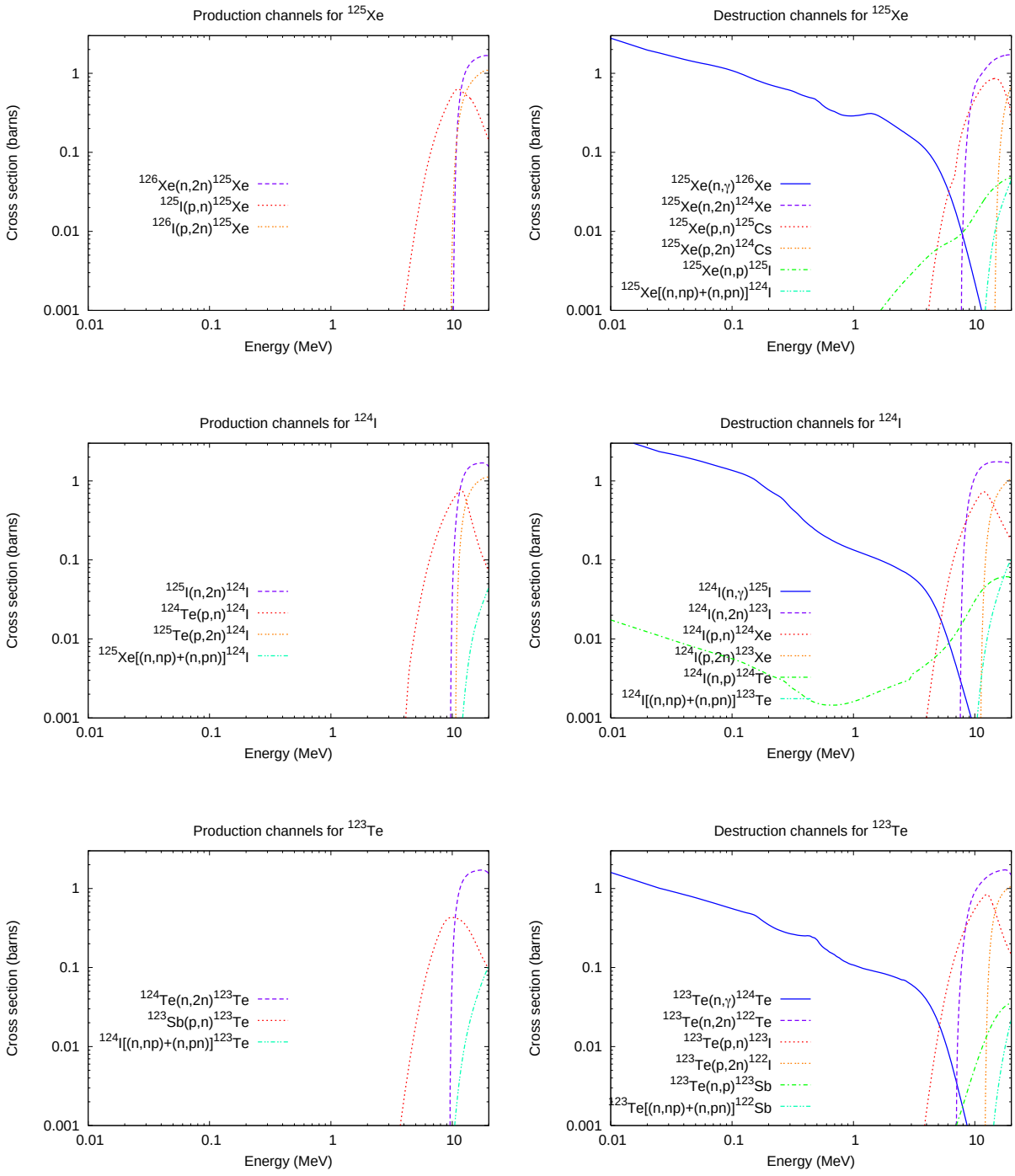

Fig. 31.— Production and destruction cross sections for N=71 target nuclei

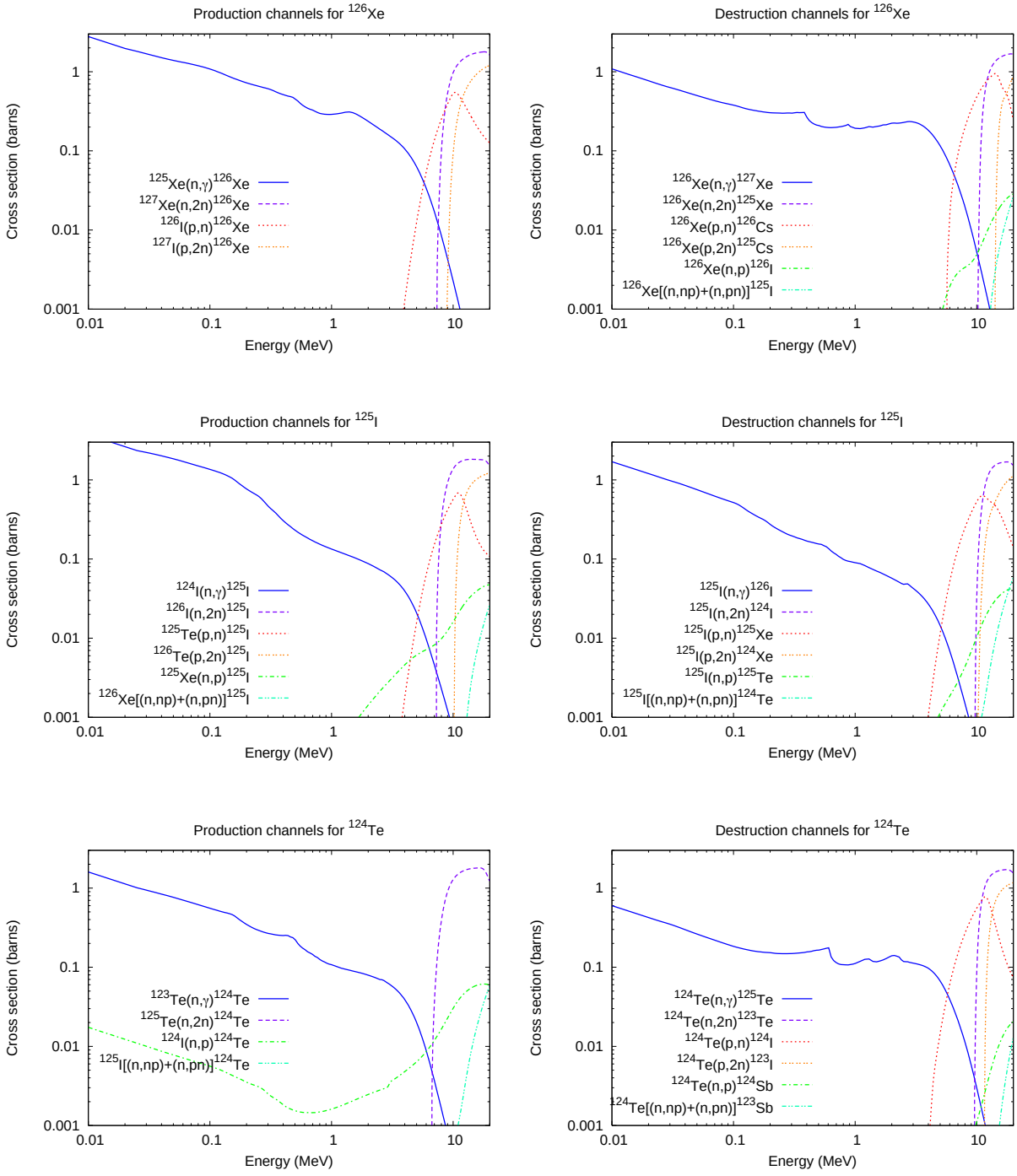

Fig. 32.— Production and destruction cross sections for N=72 target nuclei

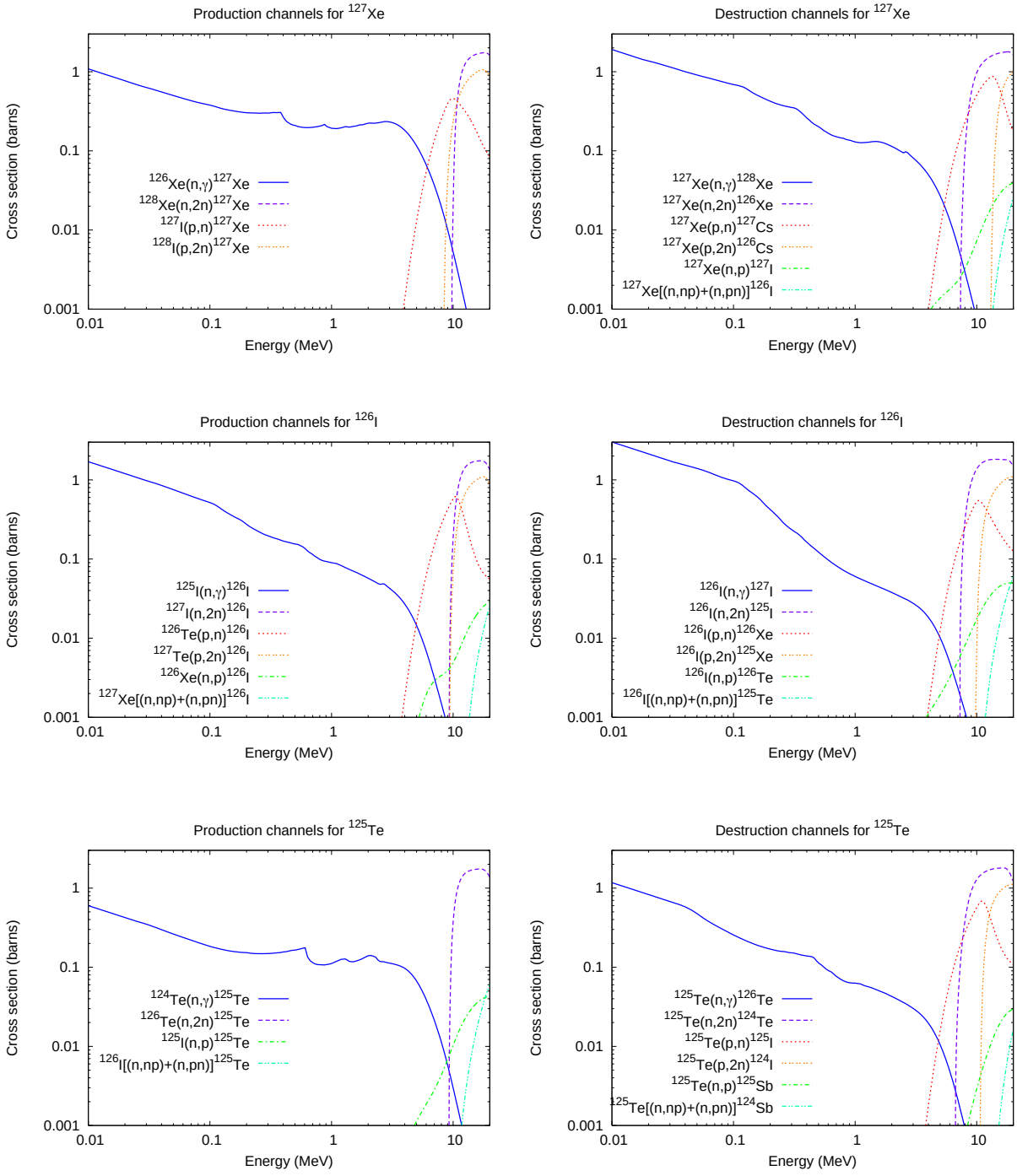

Fig. 33.— Production and destruction cross sections for N=73 target nuclei

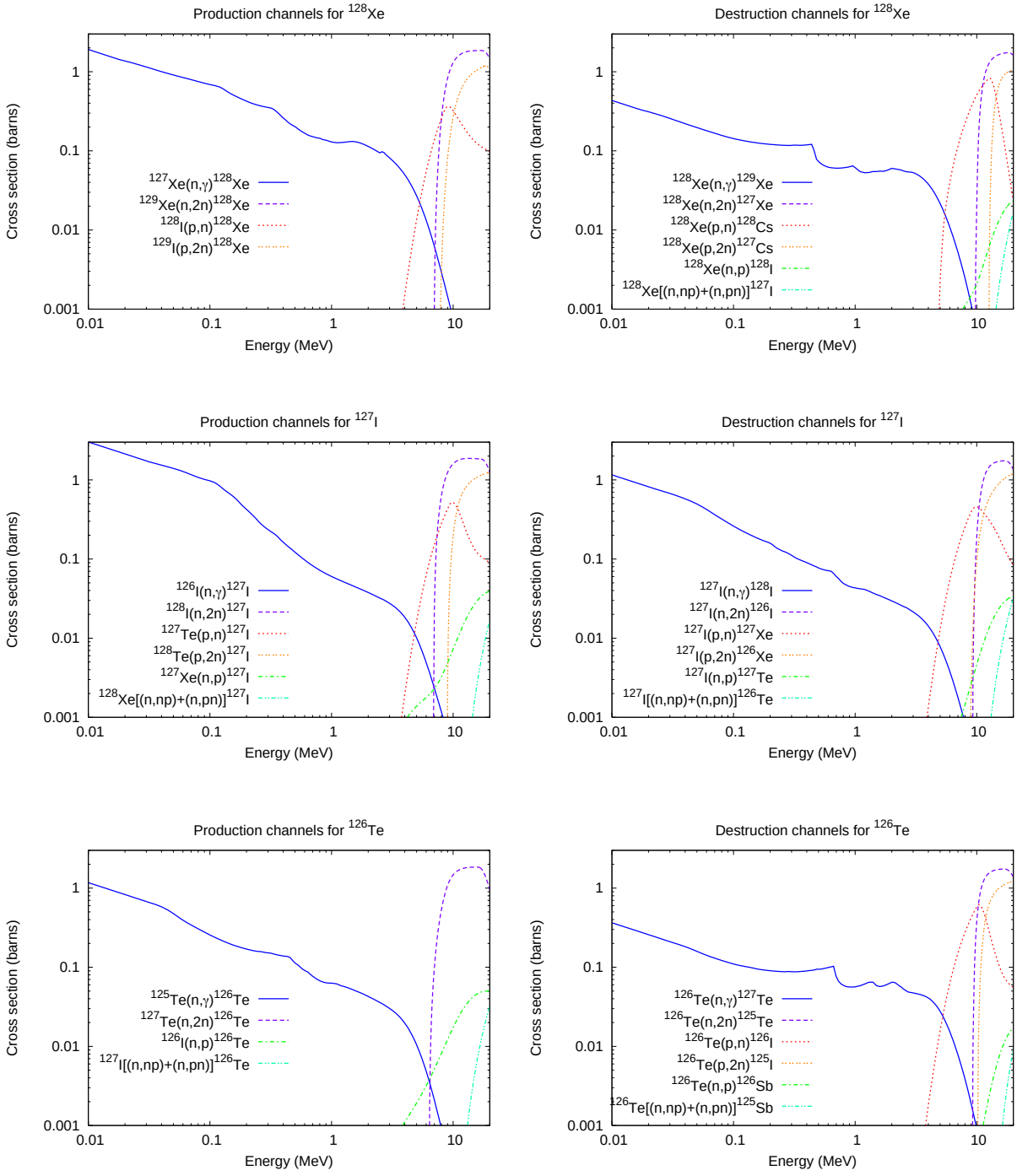

Fig. 34.— Production and destruction cross sections for N=74 target nuclei

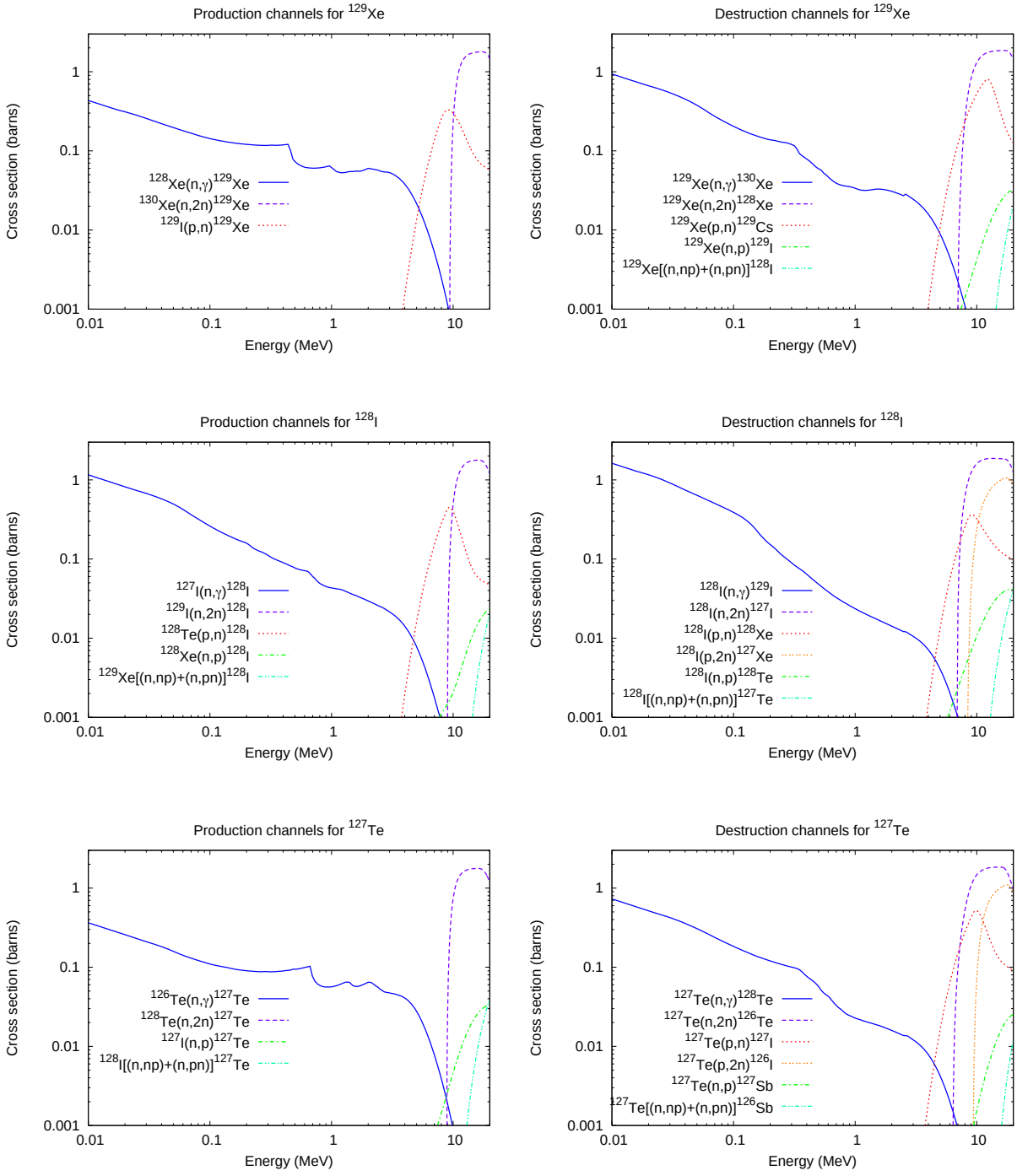

Fig. 35.— Production and destruction cross sections for N=75 target nuclei

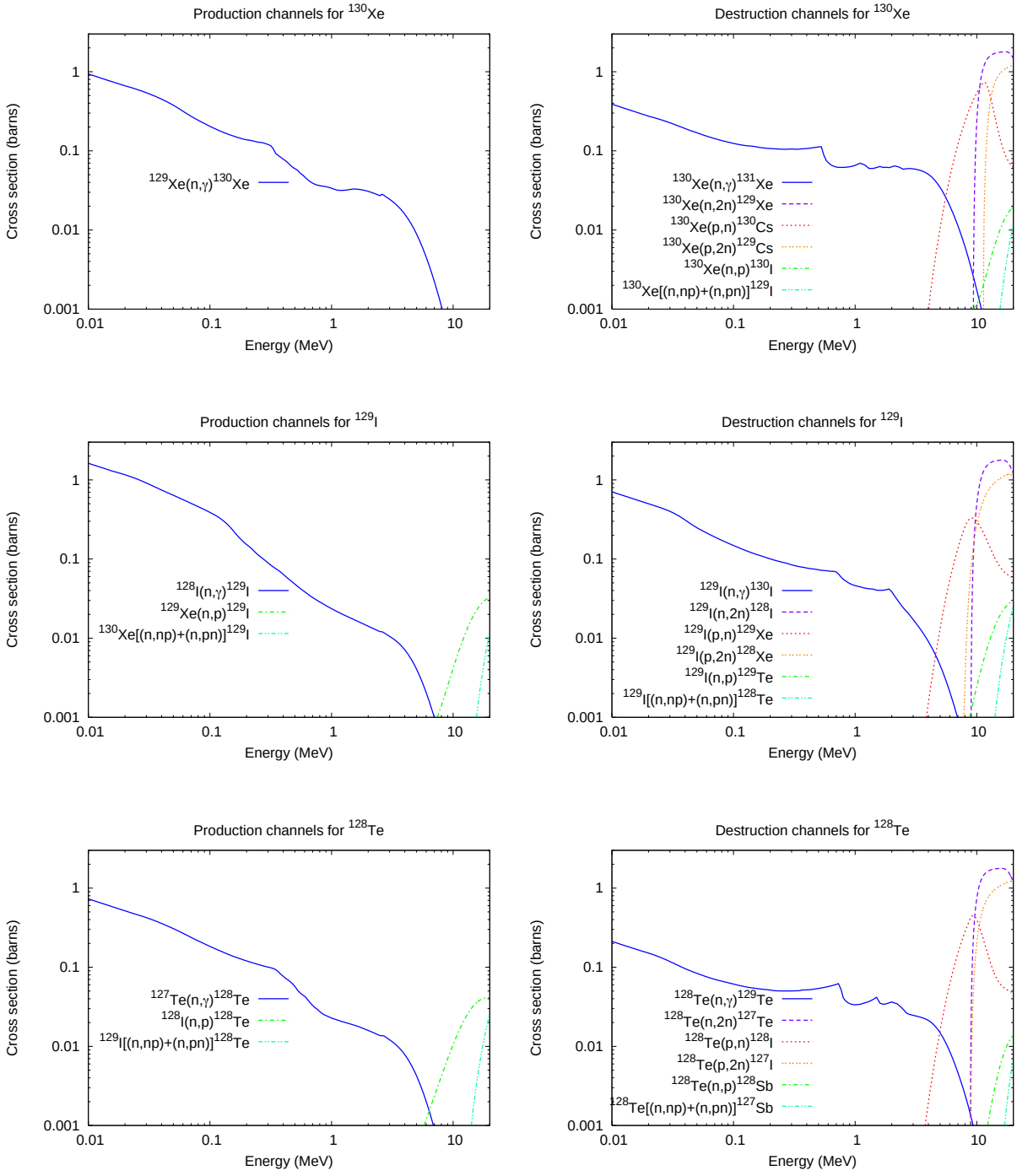

Fig. 36.— Production and destruction cross sections for N=76 target nuclei